1 **Sources, transport and visibility impact of ambient submicrometer particle size**
2 **distributions in an urban area of central Taiwan**
3

4   Li-Hao Young [a, *], Chih-Sheng Hsu [a], Ta-Chih Hsiao [b], Neng-Huei Lin [c], Si-Chee
5   Tsay [d], Tang-Huang Lin [e], Wen-Yinn Lin [f], Chau-Ren Jung [g]
6

7   [a]Department of Occupational Safety and Health, China Medical University, 100, Sec.
8   1, Jingmao Rd., Beitun Dist., Taichung 406040, Taiwan
9   [b]Graduate Institute of Environmental Engineering, National Taiwan University, 1,
10   Sec. 4, Roosevelt Rd., Taipei 10617, Taiwan
11 [c]Department of Atmospheric Sciences, National Central University, 300, Zhongda Rd,
12 Zhongli Dist., Taoyuan 320317, Taiwan
13 [d]NASA Goddard Space Flight Center, Greenbelt, MD 20771, USA
14 [e]Center for Space and Remote Sensing Research, National Central University, 300,
15 Zhongda Rd, Zhongli Dist., Taoyuan 320317, Taiwan
16 [f]Institute of Environmental Engineering and Management, National Taipei University
17 of Technology, 1, Sec. 3, Chung-Hsiao E. Rd., Taipei 106344, Taiwan
18 [g]Department of Public Health, China Medical University, 100, Sec. 1, Jingmao Rd.,
19 Beitun Dist., Taichung 406040, Taiwan
20
21

22 *Corresponding author. Tel.: +886-4-2205-3366 x.6219; Fax: +886-4-2299-2147;
23 Email: lhy@mail.cmu.edu.tw (L.-H. Young)
24

Highlights:

1. Aerosol size distributions and light extinction are attributed to six sources.
2. Emission, nucleation, growth and transport of size-resolved particles are shown.
3. Ultrafine particles drive the particle number but have little effect on visibility.
4. Elevated accumulation particles (377 nm) lead to the poorest visibility.
5. Slow-moving, stagnant air and hence local emission is key to poor visibility.

Graphical Abstract:
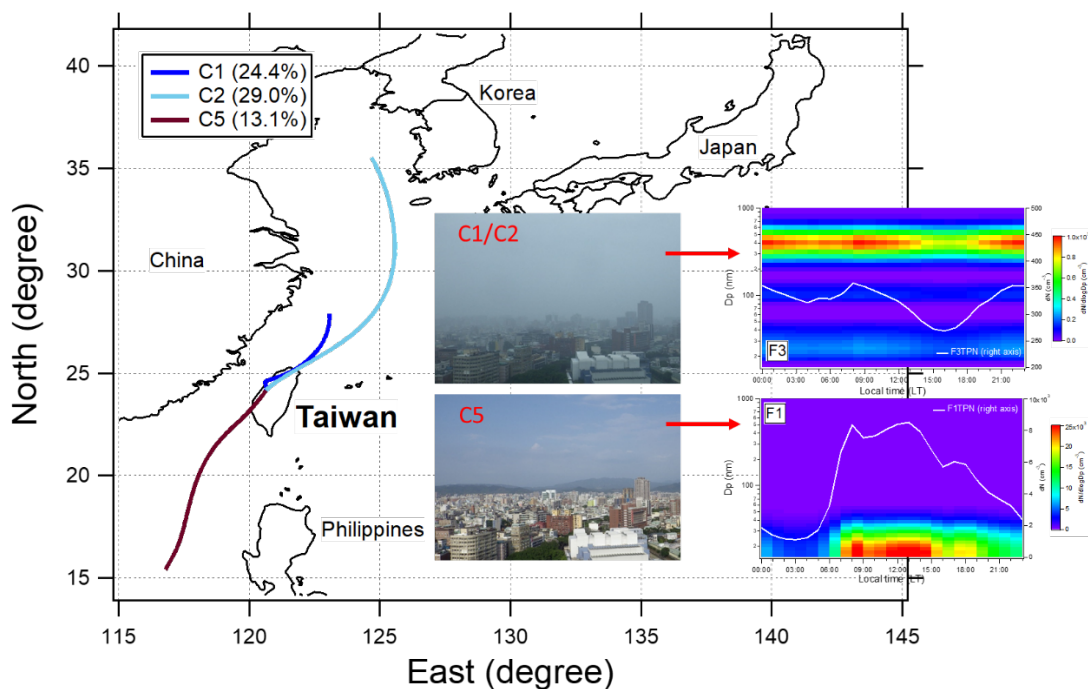
Abstract

This study used positive matrix factorization (PMF) to identify the sources of size-resolved submicrometer (10 – 1000 nm) particles and apportion their contributions to impaired visibility based on the particle number size distribution (PNSD), aerosol light extinction (b_p), and air pollutants and meteorological parameters measured over an urban basin in central Taiwan between 2017 and 2021. The transport of source-specific PNSDs was evaluated with wind and back trajectory analyses. The PMF revealed six sources of varying contributions to the total particle number (TPN), surface (TPS), volume (TPV), and b_p. Factor 1 (F1) was the key contributor to TPN (35.0%), and represented the nucleation (< 25 nm) particles from fresh traffic emission and secondary new particle formation, from the west-southwest under higher wind speed. F2 represented the large Aitken (50 – 100 nm) particles from regional transport from the north. F3 represented the elevated large accumulation (300 – 1000 nm) particles under stagnant conditions. F4 represented the small Aitken (25 – 50 nm) particles due to the growth and transport of nucleation particles of F1. F5 represented the large Aitken particles from combustion-related SO_2 source from the west-northwest. F6 represented the small accumulation (100 – 300 nm) particles from both local emission and the transport from the same SO_2 source of F5. Large accumulation particles were the major contributor to the TPV (66.4%) and TPS (34.8%), and their contribution increased markedly from 17.3% to 40.7% with decreasing visibility. Thus, particle volume and surface area are better metrices for estimating b_p. Slow-moving air masses and hence stagnant conditions play a crucial role in the build-up of elevated concentrations of accumulation mode particles, leading to the poorest visibility.

Keywords: Source apportionment, Aerosol light extinction, Regional transport, Local source, Back trajectory, Cluster analysis

1. Introduction

Atmospheric submicrometer (< 1 μm or 1000 nm) particles contribute to a major fraction of fine particulate matter or mass (PM$_{2.5}$; < 2.5 μm, referred to as FPM hereafter) (Cigánková et al., 2021; Sun et al., 2020; Y. Q. Wang et al., 2015), both of which are linked to adverse impacts on human health (Chen et al., 2017; Pope et al., 2020) and atmospheric visibility (Hand et al., 2002; Xia et al., 2017). The size distribution of submicrometer particles are commonly characterized by three modes, namely nucleation (< 25 nm), Aitken (25 – 100 nm) and accumulation (100 – 1000 nm) mode. The former two modes, together, are also known as ultrafine particles (< 100 nm). The smallest, nucleation particles are freshly-emitted or formed by combustion sources (Kumar et al., 2014; Rönkkö et al., 2017) and photochemically-driven new particle formation (Lee et al., 2019; Wang et al., 2017). During transport, atmospheric particles grow in size by coagulation or gas-to-particle conversion, thereby yielding larger particles such as Aitken and accumulation particles (Friedlander, 2000; Seinfeld and Pandis, 2016). In particular, the rate of coagulation growth increases substantially with increasing particle number concentration and particle-size difference. The growth of particles is also known as the aerosol aging process that physically and chemically transform atmospheric particles. The concentration of atmospheric particles is typically expressed by particle number (PN), surface (PS), or mass (PM), where PM is directly related to the particle volume (PV). Typically, ultrafine particles dominate the PN, whereas accumulation particles contribute substantially to PS and PV.

Due to their complex sources and dynamic nature, the particle number size distribution (PNSD) of submicrometer particles often exhibits multi-modality that varies widely in sizes and across different environments. Nevertheless, a number of source apportionment studies have attempted to resolve the source-dependent profiles of PNSD using positive matrix factorization (PMF) (Leoni et al., 2018; Masiol et al., 2016; Ogulei et al., 2007; Rivas et al., 2020; Vu et al., 2015; Yue et al., 2008). A review by Vu et al. (2015) have identified the profiles of PNSD for seven major sources, including traffic emissions, industrial emissions, biomass burning, cooking, transported aerosol, marine aerosol and nucleation. The relative contribution of each sources, as expected, depends on the sources and meteorology specific to the study location, as well as the measurement site in relation to the major sources. For example, in four European cities, Rivas et al. (2020) identified five sources of submicrometer particles, including nucleation (mode diameter, 7 – 21 nm), fresh traffic (13 – 37 nm), urban (50 – 81 nm), secondary (93 – 294 nm), and biogenic (100 nm). In addition, they were able to split the nucleation factor into photo-nucleation and traffic-nucleation sources. More specific sources could be identified when the

source apportionment includes PNSD of wider size range and other constraining variables, such as aerosol chemical composition, particulate and gas pollutants, and is supplemented with the analysis of wind speed and direction. For example, in US Baltimore, Ogulei et al. (2006) identified rather specific sources of atmospheric particles, including oil-fired power plant, secondary nitrate, local gasoline traffic, coal-fired power plant, secondary sulfate, diesel emissions/bus maintenance, wildfire episode, nucleation, incinerator, airborne soil/road-way dust, and steel plant emission.

The relationship between degraded atmospheric visibility and air pollutants, especially aerosols, has been widely reported worldwide (Hu et al., 2017; Li and Martin, 2018; Singh et al., 2017) and in recent years more extensively in Asia, especially China (Abdullah et al., 2020; Hu et al., 2021; Santoso et al., 2022; Ting et al., 2021; P. Wang et al., 2015; Yi et al., 2020). Most of the visibility studies have relied on the bulk aerosol mass (i.e., FPM and PM_{10}) and composition to establish the potential relationships. For example, the US IMPROVE algorithm has been widely used for the estimation of light extinction from light scattering and absorption by aerosols (b_{sp} and b_{ap}, respectively) and gas (b_{sg} and b_{ag}, respectively) (Malm et al., 1994; Pitchford et al., 2007). Although particle size is one of the key parameters in aerosol light extinction ($b_p = b_{sp} + b_{ap}$) estimation, the use of PNSD in visibility studies has been considerably less mainly due to the lack of information on size-resolved aerosol composition, with which the refractive index and hence aerosol light extinction could be estimated via Mie theory (Eldering et al., 1994). In China and Germany, studies have shown the decrease of visibility was associated with the increase of PNSD with modal diameters larger than 300 nm (Bäumer et al., 2008; Sun et al., 2016). In the western US, Hand et al. (2002) have reported that the accumulation mode particles were responsible for 80% of the b_{sp}. The above results are consistent with Mie theory, in which aerosols of sizes comparable to the wavelength of visible light (300 – 700 nm) are most effective, per unit volume or mass, in reducing visibility.

The above application of source apportionment is crucial for obtaining information on the origin, characteristics, and relative contributions of air pollutants, which are critical elements of effective air pollution management policies (Belis et al., 2019). In the source apportionment of PNSD, the particle size-resolved source profiles provide considerably more details of the potential atmospheric processes affecting the dynamics and evolution of aerosol size distribution (Beddows et al., 2014; Morawska et al., 1999). Compared to bulk information, this particle size-specific or modality information is especially relevant to the assessment and control of aerosols because aerosol behaviors in the environment are size-dependent, and different sources generate different characteristic sizes and concentrations of aerosols.

141   In addition to the PNSD, the inclusion of collocated air quality, aerosol composition
142 and meteorological data in the source apportionment provides constraints and reduces
143 rotational ambiguity in the PMF, thus increasing our ability to separate and identify
144 the sources (Emami and Hopke, 2017; Rivas et al., 2020). Further coupling the PMF
145 results with wind and trajectory analyses leads to refined information on the
146 directionality of sources, as well as local vs. regional sources (Petit et al., 2017). In
147 specific, wind analysis is more appropriate for assessing short-range transport,
148 whereas air mass trajectory is more applicable to long-range transport and the
149 influence of synoptic weather.

150   In the latest review, Hopke et al. (2022) identified 55 publications on source
151 apportionment of PNSDs in 102 locations/time periods. None of them further links to
152 atmospheric visibility, and none came from Taiwan. Measurements of PNSD of
153 atmospheric aerosols in Taiwan are considerably scarce, and most of them are limited
154 to short term studies (Chen et al., 2010; Cheung et al., 2016, 2013, 2011; Lin et al.,
155 2015; Young et al., 2013, 2012). Furthermore, the application of source apportionment
156 to the long-term PNSD data has not yet been reported, largely due to the lack of long-
157 term deployment of PNSD monitors in Taiwan. The role of aerosols in visibility
158 degradation has been studied more commonly with bulk aerosol composition, less
159 with PNSD, and considerably fewer with the combination of PNSD and source
160 apportionment. With that in mind, this study aims to apply PMF to the long-term data
161 on the PNSD of submicrometer particles, aerosol light extinction (b_p), air pollutants
162 and meteorology measured over an urban area in Taiwan between 2017 and 2021. The
163 PMF results are evaluated for source identification and b_p contribution, and then
164 coupled with wind and trajectory analyses for implications of source regions and
165 transport of atmospheric submicrometer particles.

166
167 **2. Methods**
168 **2.1 Study location and duration**
169   The study area was at the urban basin of Taichung City (**Fig. S1**), which is the
170 2nd most populous city with 2,801,069 residents in central Taiwan. Geographically,
171 Taichung urban basin (shaded circle in **Fig. S1**) is surrounded by hills with elevation
172 of a few hundred meters to the north, west and south, whereas the highest and largest
173 terrain in Taiwan, the Central Mountain Range, lies closely to the east of the urban
174 basin. As a result, the dispersion of air pollutants is typically suppressed. There are a
175 number of stationary sources surrounding the urban basin, in addition to the obvious
176 traffic in the urban area. Nearby stationary sources include industrial and science
177 parks, and further away near the coastline, about 17 km to the northwest of the main
178 sampling site, there is a coal-fired power plant (5500 MW), a steel plant, a harbor and

179   a few more industrial parks. It is notable that major stationary sources are more

180   concentrated to the northwest of the study area (shaded rectangle in **Fig. S1**). The

181   main sampling site (red star in **Fig. S1**) was located nearby the urban center, next to

182   one of the Taiwan EPA air quality monitoring stations, Zhongming (ZM) station (24°

183   8' 60"N, 120° 38' 24"E), on the rooftop of a school with a sampling height of 17.5 m

184   above ground level (magl). Measurements of the PNSD in the size range of 10 to

185   1094 nm were made at the main sampling site, whereas the data on criteria air

186   pollutants and meteorological parameters were obtained from the Taiwan EPA-

187   operated ZM station (described in the following Section 2.2.3). About 6 km to the

188   northwest of the main sampling site was another satellite site (red circle in **Fig. S1**),

189   where the aerosol light scattering (b_{sp}) and absorption (b_{ap}) measurements were made

190   with an air-conditioned trailer at a sampling height of 10 magl. The study campaign

191   took place between Sept. 5, 2017 to Jul. 31, 2021, resulting to a total of about 540

192   sampling days and hence 12,967 hours of data. The data coverage in each season was

193   as follows: 24% spring, 11% summer, 22% fall and 33% winter.

194

195   **2.2 Instrumentation**

196   *2.2.1 Particle number size distribution (PNSD) measurement*

197   A sequential mobility particle sizer and condensation particle counter (SMPS/CPC)

198   system (Model 5.500, GRIMM) (Heim et al., 2004) was used to continuously measure

199   the particle number size distributions (PNSDs) of dried submicrometer particles

200   through a diffusion dryer. The SMPS/CPC system consists of a long Vienna-type

201   differential mobility analyzer (L-DMA; Model 5.5-900, GRIMM) and a butanol-

202   based condensation particle counter (Model 5.403, GRIMM). Measurements were

203   made every 15 min with a sheath and sample flow rate of 3 and 0.3 L min^{-1},

204   respectively, during which the L-DMA sequentially step down high-voltage from

205   10,000 to 5 V. Thus, the detectable aerosol mobility diameters ranged from 10 to 1094

206   nm (89 size bins). The saturator and condensor temperature of the CPC was set at

207   40°C and 15°C, respectively. The CPC has a 50 % counting efficiency at 4.5 nm and

208   measures number concentration up to 2×10^4 cm^{-3} with single particle counting and

209   coincidence correction, and up to 10^7 cm^{-3} with the photometric mode. The SMPS

210   The DMA and CPC efficiencies were considered in the data acquisition and inversion

211   software (GRIMM 5.477 Version 1.35 Build 1). The sizing accuracy of the DMA was

212   validated with polystyrene latex spheres of known sizes, and the CPC was calibrated

213   in-house using a Faraday cup electrometer (FCE; Model 5.705, GRIMM) and

214   annually by the manufacturer. The measured size distribution data was first screened

215   for outliers using the generalized extreme studentized deviate procedure proposed by

216   Yu et al. (2004). Following, the mobility sizes of particles were converted to

aerodynamic size assuming spherical shape and a particle density of 1.5 g cm^{-3}. The resulting aerodynamic sizes ranged from 13 to 1,340 nm.

2.2.2 Aerosol light extinction (bp) measurement

The aerosol light scattering (b$_{sp}$) of FPM (i.e., PM$_{2.5}$) was measured with an integrating nephelometer (Model 3563, TSI) at three wavelengths of 450, 550 and 700 nm, and only the b$_{sp}$ at 550 nm at which human vision is most sensitive. A seven-wavelength aethalometer (AE33, Magee Scientific) was used to measure the aerosol light absorption (b$_{ap}$) of FPM at the wavelengths of 370, 470, 520, 590, 660, 880 and 950 nm. The b$_{ap}$ at 550 nm was interpolated using the absorption Ångström exponent (AAE) at 370 nm and 880 nm as follows.

$$AAE = -\frac{\ln[b_{ap}(370)/b_{ap}(880)]}{\ln(370/880)} \qquad (6)$$

$$b_{ap}(550) = b_{ap}(880)\left(\frac{550}{880}\right)^{-AAE} \qquad (7)$$

In this study, the aerosol light extinction (b$_p$ in Mm^{-1}) is the sum of b$_{ap}$ and b$_{sp}$, ignoring the light scattering and absorption by gases. It is important to note that the above b$_p$ is more representative of the "dry" condition due to the heating effect from the halogen lamp inside the nephelometer (Fierz-Schmidhauser et al., 2010).

2.2.3 Criteria pollutants and meteorological conditions

The Taiwan EPA-operated ZM station is equipped with β-ray attenuation monitors for FPM and PM$_{10}$ (Met One BAM-1020; WINS impactor for PM$_{2.5}$), a UV fluorescence spectrometer for SO$_2$ (Ecotech 9850B), a IR analyzer for CO (Horiba APMA-360), a chemilluminescence detector for NOx (= NO + NO$_2$) (Ecotech 9841B) and a nondispersive UV photometer for O$_3$ (Ecotech 9810B). In addition, it also houses a suite of metrological instruments for measurements of ambient temperature, relative humidity (RH) (Met One 083D), wind speed (WS) (Met One 014A), wind direction (Met One 024A), and ultraviolet index (UVI). The station is routinely maintained and audited by the Taiwan EPA in accordance to the quality assurance and control procedures outlined in the US EPA Order 5360.1.

2.3 Source apportionment: MDL, uncertainty, missing value

The PMF was carried out using an IGOR-based Source Finder (SoFi; v8.04) package developed by Canonaco et al. (2013), along with the Multilinear Engine (ME-2; v1.345) developed by Paatero (1999). The principles of PMF could be found

253   in detail elsewhere (Paatero, 1999, 1997; Paatero and Hopke, 2009). The source
254   apportionment process involved the preparation of the concentration and uncertainty
255   matrixes, described as follows. The input variables for the PMF included the PNSD,
256   b_{sp}, b_{ap}, coarse particulate matter (CPM = $PM_{10} - PM_{2.5}$), FPM (i.e., $PM_{2.5}$), SO_2, O_3,
257   NO, RH, WS and UVI. For the PNSD, the particle number (PN) concentrations were
258   averaged over three consecutive size bins and hence merged into one larger size bin to
259   reduce the measurement noise as well as the number of size-distribution variables
260   (Masiol et al., 2016). As a result, the number of size bins was reduced from 89 to 41.
261   To match the time resolution of all variables, the PNSD, b_{sp} and b_{ap} were averaged to
262   hourly data. The final data matrix (n × m) consisted of 51 variables and 12,967 hourly
263   observations.
264   The estimation method for the uncertainty data matrix was adopted and modified
265   according to earlier studies (Ogulei et al., 2006; Ogulei et al., 2007; Vu et al., 2015),
266   as follows.
267
268
$$\sigma_{ij} = \alpha_j \cdot \left(N_{ij} + \bar{N}_j \right)$$

269
270   where the σ_{ij} and N_{ij} is the estimated measurement uncertainty and the measured PN
271   concentration or other supplemental variables, respectively, for size bin or variable j
272   and sample i. For the PNSD, the α_j is the counting uncertainty estimated with the
273   inverse of $\sqrt{C}$, in which the C is the raw particle count. **Fig. S2** shows the size-
274   dependent scaled-α_j in this study. The $\bar{N}_j$ is the average concentration of PN or
275   average value of other supplemental variables for size bin or variable j. If N_{ij} equals to
276   zero, the σ_{ij} is defined as $2\bar{N}_j$. The overall uncertainty (s_{ij}) for each observation was
277   determined using the following equation.
278
279
$$s_{ij} = \sigma_{ij} + C_3 \left(N_{ij} \right)$$

280
281   where the C_3 is a constant. The α_j and C_3 could empirically determined such that the
282   scaled residuals are randomly distributed between −3 and 3, the robust object function
283   Q is close to the theoretical Q, and the model provides the most physically
284   interpretable results (Ogulei et al., 2006; Rivas et al., 2020). Accordingly, the α_j
285   mostly ranged between 0.02 and 0.08, except for the large size bins (0.12 – 0.28), and
286   $C_3 = 0.1$.
287   In the SoFi, missing values in the concentration matrix were assigned with 1000
288   times the highest uncertainty to avoid the effect of missing values on the PMF results.
289   In addition, the uncertainty matrix is further weighted cell-wise on the basis of the
290   signal to noise ratio (S/N). The uncertainty is downweighed separately for each

291 datapoint using the two-step function (Paatero and Hopke, 2003). The "weak" and
292 "bad" S/N threshold was set at 3 and 1.2, with the weighting factor of 3 and 10,
293 respectively. The PMF was run with the robust mode with a threshold of 4 to prevent
294 the PMF runs drifting away due to outliers. The sum of each factor profile over time
295 was normalized to one during the iteration, with a threshold of 0.01. The global F_{peak}
296 was used to evaluate the rotational ambiguity in the range of -1 to 1 with the step
297 interval of 0.1, and thus resulting to a total of 21 solutions for each run. The solution
298 with five factors was determined to be more reasonable and physically interpretable in
299 the study area.
300
301 **2.4 Local wind and long-range air mass trajectory**
302 An IGOR-based ZeFir package, developed by Petit et al. (2017), was used to
303 investigate the potential transport of submicrometer particles utilizing the local wind
304 speed (WS) and direction measured on-site and the long-range air mass trajectory.
305 Near-range (local) transport was evaluated using the non-parametric wind regression
306 (NWR) plot that couples wind data and pollutant concentrations to identify wind
307 sectors and hence source regions associated with elevated concentrations (Henry et
308 al., 2009). Long-range transport was evaluated using the Hybrid Single Particle
309 Lagrangian Integrated Trajectory (HYSPLIT) model (Stein et al., 2015). Hourly 72-hr
310 air mass back trajectories arriving at one-half of the mixed layer height (above sea
311 level) over the study area were calculated using the PC Windows-version HYSPLIT
312 model with the Global Data Assimilation System 1° global meteorological data. The
313 ZeFir package was used as an interface to initiate the built-in cluster analysis in the
314 HYSPLIT model and to analyze and plot the model outputs. The optimum number of
315 clusters was determined by evaluating the change of the total space variance (TSV) in
316 relation to the number of clusters. A total of five clusters was selected in this study.
317
318 **3. Results and Discussion**
319 **3.1 Overview of the meteorology and air quality**
320 The seasonal synoptic weather typical to the study area and in Taiwan are
321 described in details elsewhere (Cheng, 2001; Hsu and Cheng, 2019). The
322 meteorological conditions and air quality during the study period are given in **Table
323 S1**. The average ambient temperature, RH, wind speed (WS) and ultraviolet index
324 (UVI) were 23.1 °C, 69.1%, 1.5 m s^{-1} and 1.4, respectively, during the 2-year study
325 period in Taichung. The prevailing wind direction was southwesterly winds during the
326 summer, and north and northeasterly winds during the other three seasons (not
327 shown). It is notable that about 52% of the time the WS was less than 1.5 m s^{-1},
328 suggesting stagnant conditions are quite common in the urban area, due to its basin

geology and surrounding elevated terrain that impede air flow movement. The average coarse particulate matter (CPM = PM_{10} – $PM_{2.5}$), FPM (i.e., $PM_{2.5}$), SO_2, O_3, and NO concentrations were 16.3 µg m^{-3}, 20.3 µg m^{-3}, 2.2 ppb, 27.9 ppb, and 3.7 ppb, respectively.

Also shown in **Table S1** are the summary statistics of the size-fractionated particle number concentrations (PN). The average PN of the nucleation mode (< 25 nm) and Aitken mode (25 – 100 nm) particles (PN_{25} and PN_{25-100}, respectively) were 7.0×10^3 cm^{-3} and 6.9×10^3 cm^{-3}, respectively. The two together, known as the ultrafine particles (< 100 nm), contributed to 86% of the average total PN (TPN; 16.3×10^3 cm^{-3}). The average PN of the accumulation mode particles (100 – 1000 nm) was 2.4×10^3 cm^{-3}, contributing to 14% of the TPN. It is notable that the above size-dependent contributions to the TPN are nearly identical to the results of an earlier study at the same urban area between 2008 and 2010, during which the average TPN was 34.2×10^3 cm^{-3} (Young et al., 2012). This shows that the size-fractionated PN in this study have reduced by a factor of about 2 from that observed PN more than a decade ago.

Table 1 shows that the averages of the observed b_{sp}, b_{ap} and b_p were 65.2, 22.9 and 88.3 Mm^{-1}, respectively, with the b_{sp} contributing to 74% of the b_p. The b_p of this study is about 10-fold lower than that observed in Beijing, China (Hu et al., 2021). To facilitate the discussion with visibility, the data was divided into four quarters (Q1, Q2, Q3 and Q4) according to the first (25% percentile), second (50%) and third (75%) quartiles of the b_p during the study period. As shown in **Table 1**, the b_{sp}, b_{ap} and b_p increased by a factor of more than 5 with decreasing visibility, with the b_{sp} showing the highest increase (a factor of 9.1). Clearly, the b_{sp} was the dominant factor controlling atmospheric visibility, especially under severely impaired visibility.

Fig. 1 presents the diurnal variations of aerosol parameters (CPM, FPM, b_{sp}, b_{ap}, b_p), gas pollutants (SO_2, O_3, NO) and meteorological parameters (T, RH, WS and UVI). As show, elevated FPM typically occurred in late morning (1000 – 1100 local time (LT)) and nighttime, whereas elevated CPM coincided with higher WS. The 2 – 3 hr lag between the NO and FPM peaks indicate the secondary nature of FPM. The CPM appeared to be related to wind-driven resuspension of dust. The b_{ap} in the morning appeared to follow closely with the NO, thus indicating the connection between b_{ap} and direct traffic emission. This is consistent with the fact that the major light absorbing carbon in aerosols is the black carbon from incomplete combustion (Briggs and Long, 2016). Unlike the b_{ap}, the lack of NO peak during the late afternoon rush-hour was due to the enhanced atmospheric dilution and NO titration with oxidants (e.g., O_3). The peak of O_3 lagged about 2 hr after the peak of UVI.

3.2 Source profiles of particle number, surface and volume

The PMF-reconstructed TPN were in good agreement with the observed TPN, with the Deming regression slope of 0.85 and R^2 of 0.97 (**Fig. 2**). The Deming regression differs from the ordinary least square regression in that the errors in both the dependent and independent variables are considered by the former method. The PMF-resolved six PNSDs were then converted to particle surface and volume size distributions (PSSDs and PVSDs, respectively) assuming spherical particles.

Fig. 3 shows the PMF-resolved particle number, surface and volume size distribution profiles of the six factors (i.e., potential sources) and their contributions to the TPN, total surface (TPS) and volume (TPV). Factor 1 (F1), F4 and F5 dominated the TPN, contributing to 35.0%, 28.1%, 20.9% of the TPN, respectively. The three together made up 84.0% of TPN, and all showed elevated concentrations of ultrafine particles (< 100 nm). More specifically, the mode diameter of F1 was in the nucleation mode size range. The mode diameter of F4 was at the lower end of the Aitken mode (25 – 50 nm; referred to as "small" Aitken mode hereafter), whereas that of F5 was at the higher end of the Aitken mode (50 – 100 nm; referred to as "large" Aitken mode hereafter). F6 contributed to only 10.0% of the TPN, whereas the remaining factors F2 and F3 each contributed to less than 4.0% of the TPN. F6 had a more obvious particle mode at the lower end of the accumulation mode (100 – 300 nm; referred to as "small" accumulation mode hereafter), whereas F3 had a mode at the higher end of the accumulation mode (300 – 1000 nm; referred to as "large" accumulation mode hereafter). Similar to F1, F4 and F5, F2 had a mode in the large Aitken mode but with considerably lower concentration.

With respect to the TPS, F6, F3 and F5 showed the most significant contributions, together they made up 89.7% of the TPS. The mode diameter of F6 was in the small accumulation mode, whereas that of F3 was in the large accumulation mode. The remaining factors F4, F2 and F1 each contributed to less than 5.7% of the TPS. With respect to the TPV, F3 and F6 together contributed to 90.2% of TPS. The mode diameter of F3 was in the large accumulation mode, whereas that of F6 was in the small accumulation mode. The remaining factors F5, F2, F4 and F1 each contributed to less than 7.4% of the TPV. The above results suggest that F1, F4 and F5 are important to TPN, whereas F6, F3 and F5 are important to TPS, and F3 and F6 are important to TPV. Unlike others, F2 had rather minor contributions to either TPN, TPS, or TPV. This suggests that F2 is likely representative of transient particles during transport or aerosol growth processes.

3.3 Source interpretations.

Fig. 4 gives the diurnal variation of the PMF-resolved average PNSD and TPN,

405　factor loading and non-parametric wind regression (NWR) plot of F1, F2 and F3.

406　Only PN is shown here because the temporal trends of particle surface and volume are

407　exactly the same as that of PN (**Fig. S3**). A summary of the PN mode, mode diameter,

408　peak PN hour, source region and wind condition for each of the identified source

409　types is given in **Table 2** and discussed in the following.

410　　　For F1, the PNSDs exhibited unimodal distribution and were characterized by a

411　distinct particle mode at 16 nm. In addition, F1 had low loadings on both the air

412　pollutants and meteorological parameters, but NO and UVI, which is an indicator of

413　traffic emission and strong photochemistry, respectively. Due to their small sizes, as

414　expected, F1 showed negligible loadings on particle mass (CPM and FPM) and

415　aerosol light extinction (b_{sp} and b_{ap}). As the largest contributor to TPN, F1 shows the

416　strongest diurnal pattern in which its TPN (F1TPN) began increasing sharply after

417　sunrise at 0600 LT and reaching the first peak at 0800 LT, and then the second peak at

418　1300 LT. Those two peaks coincided with the traffic-related NO and photochemically-

419　driven O_3 (**Fig. 2**). This indicates that F1 is a mixture of primary emission and

420　secondary formation of nucleation mode particles. Numerous studies have shown that

421　the two major sources of elevated nucleation mode particles are primary traffic

422　emission and photochemically-driven secondary new particle formation (Lee et al.,

423　2019; Morawska et al., 2008; Young et al., 2013, 2012). However, the Pearson

424　correlation coefficients (*r*) of the F1TPN with NO and UVI were 0.13 and 0.40,

425　respectively (**Table 3**). The low r with NO, in particular, was rather unexpected and

426　likely due to the PMF unable to resolve the two major sources that almost overlap

427　temporally with each other in the morning. Hopke et al. (2022) reported the common

428　two-peaks feature of this source type, associated with morning traffic and secondary

429　formation in the afternoon. The NWR plot reveals that there is a clear source region to

430　the west-southwest of the monitoring site. A follow up source review identified that

431　there are a high-traffic intersection and an expressway ramp in that region where

432　traffic is frequently congested. Thus, it is more likely that F1 is attributable to the

433　transport of nucleation mode particles from primary (fresh) traffic emission and

434　secondary new particle formation under higher wind speed (~ 8 km hr^{-1} or 2.2 m s^{-1}).

435　　　For F2, the PNSDs exhibited trimodal distribution and were characterized by a

436　more prominent mode at 69 nm. In addition, F2 showed high loadings on most air

437　pollutants and meteorological parameters, despite its minor contributions to TPN, TPS

438　and TPV. This suggests that F2 is representative of the overall air quality and

439　meteorology in the study region. In particular, the highest loadings were on O_3 and

440　WS. The F2TPN began increasing gradually from 0700 LT and reached a maximum at

441　1600 LT, closely following the diurnal variation of the wind speed (**Fig. 2**). The *r*

442　between the F2TPN and O_3 was only -0.06, but the *r* with NO and WS were –0.42 and

443 0.56, respectively (**Table 3**). Along with the NWR plot, these results suggest that
444 northerly winds are conducive to wind-driven, regional transport of large Aitken mode
445 particles. A very similar factor with a mode diameter of 75 nm was identified by
446 Leoni et al. (2018), who attributed to the wind-driven regional pollution.

447 　　For F3, the PNSDs exhibited trimodal distribution and were characterized by a
448 more prominent mode at 377 nm. In addition, F3 showed high loadings on b_{sp} and
449 FPM. The F3TPN had a maximum at 0800 LT and then continuously decreased to a
450 minimum at 1600 LT (**Fig. 2**). In addition, the F3TPN was generally higher during
451 nighttime than daytime. The r of the F3TPN with b_{sp} and FPM were 0.65 and 0.64,
452 respectively (**Table 3**). These relatively strong correlations are consistent with the fact
453 that F3 was the major contributor to TPV and TPS, and hence FPM. The FPM is well
454 known to dominant aerosol light scattering (Deng et al., 2014; Pitchford et al., 2007).
455 The NWR plot indicates that elevated F3TPN were more limited to stagnant
456 conditions (< 4 km/hr or 1.1 m s^{-1}). Thus, F3 is representative of the build-up of local
457 aged, large accumulation mode particles under stagnant conditions.

458 　　**Fig. 5** gives the diurnal variation of the PMF-resolved average PNSD and TPN,
459 factor loading and non-parametric wind regression (NWR) plot of F4, F5 and F6. For
460 F4, the PNSDs exhibited unimodal distribution and were characterized by a mode
461 diameter of 40 nm. In addition, similar to F1, F4 had low loadings on both the air
462 pollutants and meteorological parameters. The diurnal variation and NWR plot of
463 F4TPN were also very similar to F1TPN. The r between the two factors was 0.45
464 (**Table 3**). The major difference between the two was their PNSDs, between which the
465 mode diameter of F4 was larger than that of F1. This suggests that F4 represents the
466 growth process from nucleation mode to small Aitken mode particles.

467 　　For F5, the PNSDs exhibited unimodal distribution and were characterized by a
468 mode diameter of 84 nm. In addition, F5 had relatively higher loadings on b_{ap} and
469 SO$_2$. The r of the F5TPN with b_{ap} and SO$_2$ were 0.67 and 0.49, respectively (**Table 3**).
470 The relatively strong association with b_{ap} indicates fossil-fuel combustion sources
471 because the major contributor to b_{ap} is known to be black carbon. The F5TPN had
472 three distinct maxima at 0800, 1200 and 2000 LT, respectively. Similar to F1, the first
473 peak at 0800 LT was likely related to traffic emission (**Fig. 2**). The second peak at
474 1200 LT, the smallest among the three peaks, was more difficult to explain but may be
475 associated with the growth and/or transport of aerosols. The third peak at night was
476 the most prominent feature of F5TPN. The NWR plot revealed that elevated F5TPN
477 was not limited to local emissions under stagnant conditions (< 1.1 m s^{-1}), but also
478 related to the transport from a source region to the west-northwest of the study site
479 under higher wind speed (> 1.1 m s^{-1}). It was found that the NWR plot of F5TPN is
480 quite similar to that of SO$_2$ (**Fig. S4**), which has a common source region as that of

481 F5. As described in Section 2.1, there are concentrated industries, a coal-fired power
482 plant and a harbor to the to the west-northwest of the study site. Therefore, F5
483 represents elevated large Aitken mode particles from a mixture of local traffic
484 emission under stagnant conditions and transport from SO_2-emitting sources under
485 higher wind speed.

486   For F6, the PNSDs exhibited bimodal distribution and were characterized by a
487 more prominent mode at 168 nm. In addition, F6 had relatively higher loadings on b_{ap},
488 FPM and b_{sp}. The diurnal variation of F6 was similar to F3, with a daytime maximum
489 at 0800 LT and a daytime minimum at 1600 LT (**Fig. 2**). Also, like F3, F6 was the
490 highest TPS contributor and the major TPV contributor. The r of the F6TPN with b_{ap},
491 FPM and b_{sp} was 0.72, 0.69, and 0.61, respectively (**Table 3**). On the other hand,
492 nearly identical to F5, the NWR plot showed that elevated F6TPN was due to local
493 emission under stagnant conditions (same as F3), and the transport from the SO_2
494 source region to the west-northwest of the study area under higher wind speed (same
495 as F5). The r between F6TPN and F5TPN (0.64) was higher than that between F6TPN
496 and F3TPN (0.50) (**Table 3**). The above results indicate that F6 was likely a result of
497 the build-up of local small accumulation mode particles under stagnant conditions,
498 and the growth of large Aitken mode particles to small accumulation mode particles.
499
500 **3.4 Impact on visibility**
501   In the PMF results, the b_p (= b_{sp} + b_{ap}) was attributed to each of the
502 aforementioned 6 sources. The reconstructed b_p were in reasonable agreement with
503 the observed b_p, with the Deming regression slope of 0.50 and R^2 of 0.61 (**Fig. S5**).
504 **Fig. 6** presents the b_p and b_p-contributions associated with the PMF-resolved six
505 factors under different visibility classes; the first quarter (Q1) represents the best
506 visibility, whereas the fourth quarter (Q4) represents the poorest visibility. As shown,
507 the b_p increased by a factor of 4.2 from Q1 to Q4. In particular, the contribution of F3
508 to the total b_p showed the largest increase with decreasing visibility, from 17.3%
509 contribution in Q1 to 40.7% contribution in Q4. Based on the profile of F3, discussed
510 previously, this suggests that the elevated large accumulation mode (300 – 1000 nm)
511 particles under stagnant condition were the main cause of the poorest visibility in the
512 study area. In addition, F6 was also important in impairing visibility, though its
513 contribution from 24.6% to 32.8% was not as significant as that of F3. In specific, F3
514 had PS and PV modes between 500 – 600 nm, whereas F6 had PS and PV modes
515 between 200 – 300 nm. Therefore, it is clear that particle surface and volume were
516 better metrics in explaining the aerosol light extinction. These findings are consistent
517 with earlier studies (Bäumer et al., 2008; Cheng et al., 2015; Hand et al., 2002; Sun et
518 al., 2016). In specific, Hand et al. (2002) showed that the accumulation mode particles

519   contributed to 80% of the total b_{sp} in a US national park, a number nearly identical to

520   the combined contribution of F3 and F6 to 79.2% of the total b_{sp} in this study. The

521   contributions of F5 were moderate and remained relatively constant at $19.3 \pm 1.1\%$

522   over different visibility classes. On other hand, the contribution of F2 showed the

523   largest decrease with decreasing visibility, from 33.9% in Q1 to 6.1% in Q4. Based on

524   the profile of F2, the regional air quality and transport of large Aitken mode particles

525   under northerly winds were associated the best visibility in the study area. Similar to

526   F2, F1 and F4 had negligible contributions to the b_p under the worst visibility.

527

528   **3.5 Effect of air mass**

529   **Fig. 7** shows the five representative clusters of 72-hr air-mass back trajectory

530   during the study period. These clusters are qualitatively consistent with those reported

531   by (Hsu and Cheng, 2019) between 2013 and 2018 in Taiwan. As shown, relatively

532   stronger northeasterly winds (cluster C2, C3 and C4) were the dominant air mass

533   trajectories, contributing to a total of 62.5% of study period. These three clusters

534   represent the eastward movement of the Asian continental high-pressure system

535   (anticyclone) from inland China to the Pacific Ocean, in the order of C4, C3 and C2,

536   during winter and fall (**Fig. S6**). Among them, the wind speed was relatively lower for

537   C2 due to the relatively weaker synoptic weather as the anticyclone moved further

538   away to the Pacific Ocean.

539   The slowest moving (stagnant) air mass trajectory from the northeast, C1,

540   contributed 24.4% of the study period. Along with its lowest wind speed, it is noted

541   that trajectory of C1 made a turn to the south while approaching the study area, and

542   thus conducive to poor dispersion and trapping of inland air pollutants against the

543   Central Mountain Range (**Fig. S1**). This cluster is representative of the weak synoptic

544   weather that often exhibits stagnant condition and strong subsidence due to terrain

545   blocking (Hsu and Cheng, 2016), particularly in the Taichung urban basin during

546   spring and summer (**Fig. S6**). The remining 13.1% of the study period was affected by

547   mild southwesterly winds of C5. This cluster is associated with the westward

548   stretching of the Pacific subtropical high-pressure system and the moist southwesterly

549   flow that often brings in higher rainfall during summer (**Fig. S6**) (Hsu and Cheng,

550   2019).

551   **Fig. 8** shows the b_p and b_p-contributions associated with the PMF-resolved six

552   factors for each air-mass back trajectory cluster. The b_p of C1 and C2 were a factor of

553   1.5 to 2.3 higher than that of the three other clusters, C3, C4 and C5. The relatively

554   slow- and southwestward-moving air masses of C1 and C2, particularly the former,

555   were conducive to poor dispersion and hence build-up of submicrometer aerosols.

556   Consistent with the findings in Section 3.3, the build-up and hence elevated

557   concentrations of large (F3) and small (F6) accumulation mode particles were the
558   main contributors to the elevated b_p of C1 and C2. F3 and F6, together, contributed to
559   60.6% to 70.0% of the total b_p. In Germany, Bäumer et al. (2008) showed that air
560   mass underwent aging process during which the number of particles larger than 300
561   nm increased and thus degraded the visibility under high-pressure systems with low
562   horizontal pressure gradient (i.e., small horizontal advection). The large Aitken mode
563   particles (F5) was the third largest contributor to the b_p. On the other hand, the lowest
564   b_p was associated with southwesterly air masses (C5). The low-pressure system,
565   originating from the South Sea, often drives the moist southwesterly winds and brings
566   in heavy rain to Taiwan during spring and summer. The stronger wind speeds of C3
567   and C4 clearly resulted in a relatively lower b_p, compared to that of C1 and C2,
568   whereas higher than that of C5.
569   It is noted that the factor contributions were relatively stable among the air-mass
570   trajectory clusters, with their standard deviations (SD) smaller than 3.7%, except for
571   F2 (SD = 6.6%). Consistent with the findings in Section 3.3, F2 showed increased
572   contribution with decreasing b_p under higher wind speeds. This indicates that the
573   relative source strength did not vary substantially under different air mass trajectories
574   and thus the elevated b_p was primarily due to the stagnant conditions associated with
575   weak synoptic weather.
576
577   **4. Conclusions**
578   The number size distributions of ambient submicrometer particles (10 – 1000 nm)
579   were measured over an urban area in central Taiwan from 2017 to 2021, along with
580   concurrent monitoring of aerosol light extinction ($b_p = b_{sp} + b_{ap}$), air quality and
581   meteorological conditions. PMF model was applied to the hourly particle number size
582   distribution (41 size bins), b_{sp}, b_{ap}, coarse particulate matter (CPM; $PM_{10} - PM_{2.5}$),
583   fine particulate matter (FPM; $PM_{2.5}$), SO_2, O_3, NO, RH, wind speed (WS) and
584   ultraviolet index (UVI). The HYSPLIT air mass trajectories and non-parametric wind
585   regression (NWR) plots were used to identify transport characteristics and source
586   regions of size-resolved submicrometer particles. The PMF-resolved six factors (or
587   sources) were able to reasonably reconstruct the particle number size distributions (R^2
588   = 0.97) and b_p ($R^2 = 0.61$). Factor 1 (F1) was the key contributor to the total particle
589   number (TPN), characterized by elevated concentrations of nucleation mode (< 25
590   nm) particles. F1 was associated with primary (fresh) traffic emission (NO) and the
591   secondary new particle formation (UVI), transported from the west-southwest region
592   of the study area under higher wind speed (> 2.2 m/s). F2 had negligible contributions
593   to TPN, total particle surface (TPS) and volume (TPV), characterized by a small
594   particle number mode at large Aitken-mode (50 – 100 nm) size range. However, it had

the strongest loadings on air pollutants and meteorology, and thus representing regional air pollution and meteorology. F2 arose mainly from wind-driven transport from the northern region of the study area. F3 was the key contributor to TPS and TPV, characterized by elevated large accumulation mode (300 – 1000 nm) particles under stagnant conditions, and thus local sources were likely more important. F4 was also a major contributor to TPN, characterized by elevated small Aitken mode (25 – 50 nm) particles due to the growth and transport of nucleation mode particles of F1 from the same source region. F5 was a moderate contributor to TPN and TPS, characterized by elevated large Aitken mode particles. The notable positive correlations of F5 with SO_2 and b_{ap} suggested it was related to the combustion of fossil fuels from the west-northwest region of the study area. Similar to F3, F6 was the major contributor to TPS and TPV, characterized by elevated small accumulation mode (100 – 300 nm) particles. F6 was representative of a mixture of local emission under stagnant condition and, similar to F5, the transport from a SO_2 source region to the west-northwest of the study area under higher wind speed.

The increased concentration and contribution of large accumulation mode particles (F3) were the main reason leading to the severely degraded visibility, followed by small accumulation (F6) and large Aitken mode (F5) particles. This indicates the positive correlation of increased b_p (i.e., decreased visibility) with increasing particle size. Although those larger particles (F3, F6 and F5) had minor to little contributions to TPN, they were the major contributors to the TPV and TPS, and showed strong correlations with FPM, b_{sp} and b_p. This suggests that the TPV and TPS were better metrices for estimating the visibility impact of submicrometer particles, whereas the TPN was a poor predictor of visibility. Interestingly, the analysis on air mass trajectory shows that the relative strength of each of the sources did not vary much with different trajectory clusters. The slow-moving air masses and hence stagnant atmospheric conditions play a crucial role in causing the build-up of elevated concentrations of accumulation mode particles, and hence impaired visibility. The abatement of accumulation mode particles from local sources, such as traffic emissions and nearby stationary sources, are the key to improving the visibility in the urban area of central Taiwan.

References

Abdullah, S., Napi, N.N.L.M., Ahmed, A.N., Mansor, W.N.W., Mansor, A.A., Ismail, M., Abdullah, A.M., Ramly, Z.T.A., 2020. Development of multiple linear regression for particulate matter (PM_{10}) forecasting during episodic transboundary haze event in Malaysia. Atmosphere 11, 289. https://doi.org/10.3390/atmos11030289

Bäumer, D., Vogel, B., Versick, S., Rinke, R., Möhler, O., Schnaiter, M., 2008. Relationship of visibility, aerosol optical thickness and aerosol size distribution in an ageing air mass over South-West Germany. Atmos. Environ. 42, 989–998. https://doi.org/10.1016/j.atmosenv.2007.10.017

Beddows, D.C.S., Dall'Osto, M., Harrison, R.M., Kulmala, M., Asmi, A., Wiedensohler, A., Laj, P., Fjaeraa, A.M., Sellegri, K., Birmili, W., Bukowiecki, N., Weingartner, E., Baltensperger, U., Zdimal, V., Zikova, N., Putaud, J.-P., Marinoni, A., Tunved, P., Hansson, H.-C., Fiebig, M., Kivekäs, N., Swietlicki, E., Lihavainen, H., Asmi, E., Ulevicius, V., Aalto, P.P., Mihalopoulos, N., Kalivitis, N., Kalapov, I., Kiss, G., Leeuw, G. de, Henzing, B., O'Dowd, C., Jennings, S.G., Flentje, H., Meinhardt, F., Ries, L., Gon, H.A.C.D. van der, Visschedijk, A.J.H., 2014. Variations in tropospheric submicron particle size distributions across the European continent 2008–2009. Atmos Chem Phys 14, 4327–4348. https://doi.org/10.5194/acp-14-4327-2014

Belis, C.A., Favez, O., Mircea, M., Diapouli, E., Manousakas, M.-I., Vratolis, S., Gilardoni, S., Paglione, M., Decesari, S., Mocnik, G., Mooibroek, D., Salvador, P., Takahama, S., Vecchi, R., Paatero, P., 2019. European Guide on Air Pollution Source Apportionment with Receptor Models: Revised version 2019. European Commission, Joint Research Centre. https://doi.org/10.2760/439106

Briggs, N.L., Long, C.M., 2016. Critical review of black carbon and elemental carbon source apportionment in Europe and the United States. Atmos. Environ. 144, 409–427. https://doi.org/10.1016/j.atmosenv.2016.09.002

Canonaco, F., Crippa, M., Slowik, J.G., Baltensperger, U., Prevot, A.S.H., 2013. SoFi, an IGOR-based interface for the efficient use of the generalized multilinear engine (ME-2) for the source apportionment: ME-2 application to aerosol mass spectrometer data. Atmos. Meas. Tech. 6, 3649–3661. https://doi.org/10.5194/amt-6-3649-2013

Chen, G., Li, S., Zhang, Y., Zhang, W., Li, D., Wei, X., He, Y., Bell, M.L., Williams, G., Marks, G.B., Jalaludin, B., Abramson, M.J., Guo, Y., 2017. Effects of ambient PM_1 air pollution on daily emergency hospital visits in China: an epidemiological study. Lancet Planet. Health, e221–e229. https://doi.org/10.1016/s2542-5196(17)30100-6

665 Cheng, W.L., 2001. Synoptic weather patterns and their relationship to high ozone
666   concentrations in the Taichung Basin. Atmos. Environ. 35, 4971–4994.

667 Cheng, Y.-C., Liang, C.-S., Syu, J.-Y., Chang, Y.-Y., Yan, Y.-L., Chen, S.-J., Chen,
668   C.-C., Lin, W.-Y., 2015. Characteristics of aerosol extinction coefficient in Taipei
669   metropolitan atmosphere. Aerosol Air Qual. Res. 15, 1823–1835.
670   https://doi.org/10.4209/aaqr.2015.03.0132

671 Chen, S.-C., Tsai, C.-J., Chou, C.C.K., Roam, G.-D., Cheng, S.-S., Wang, Y.-N.,
672   2010. Ultrafine particles at three different sampling locations in Taiwan. Atmos.
673   Environ. 44, 533–540. https://doi.org/10.1016/j.atmosenv.2009.10.044

674 Cheung, H.C., Chou, C.C.-K., Chen, M.-J., Huang, W.-R., Huang, S.-H., Tsai, C.-Y.,
675   Lee, C.S.L., 2016. Seasonal variations of ultra-fine and submicron aerosols in
676   Taipei, Taiwan: implications for particle formation processes in a subtropical
677   urban area. Atmos. Chem. Phys. 16, 1317–1330. https://doi.org/10.5194/acp-16-
678   1317-2016

679 Cheung, H.C., Chou, C.C.K., Huang, W.R., Tsai, C.Y., 2013. Characterization of
680   ultrafine particle number concentration and new particle formation in an urban
681   environment of Taipei, Taiwan. Atmos. Chem. Phys. 13, 8935–8946.
682   https://doi.org/10.5194/acp-13-8935-2013

683 Cheung, H.C., Morawska, L., Ristovski, Z.D., 2011. Observation of new particle
684   formation in subtropical urban environment. Atmos. Chem. Phys. 11, 3823–3833.
685   https://doi.org/10.5194/acp-11-3823-2011

686 Cigánková, H., Mikuška, P., Hegrová, J., Pokorná, P., Schwarz, J., Krajčovič, J.,
687   2021. Seasonal variation and sources of elements in urban submicron and fine
688   aerosol in Brno, Czech Republic. Aerosol Air Qual. Res. 21, 200556.
689   https://doi.org/10.4209/aaqr.2020.09.0556

690 Deng, J., Xing, Z., Zhuang, B., Du, K., 2014. Comparative study on long-term
691   visibility trend and its affecting factors on both sides of the Taiwan Strait. Atmos.
692   Res. 143, 266–278. https://doi.org/10.1016/j.atmosres.2014.02.018

693 Eldering, A., Cass, G.R., Moon, K.C., 1994. An air monitoring network using
694   continuous particle size distribution monitors: Connecting pollutant properties to
695   visibility via Mie scattering calculations. Atmos. Environ. 28, 2733–2749.
696   https://doi.org/10.1016/1352-2310(94)90445-6

697 Emami, F., Hopke, P.K., 2017. Effect of adding variables on rotational ambiguity in
698   positive matrix factorization solutions. Chemom. Intell. Lab. Syst. 162, 198–202.
699   https://doi.org/10.1016/j.chemolab.2017.01.012

700 Fierz-Schmidhauser, R., Zieger, P., Wehrle, G., Jefferson, A., Ogren, J.A.,
701   Baltensperger, U., Weingartner, E., 2010. Measurement of relative humidity

702 dependent light scattering of aerosols. Atmos. Meas. Tech. 3, 39–50.

703 https://doi.org/10.5194/amt-3-39-2010

704 Friedlander, S.K., 2000. Smoke, Dust, and Haze: Fundamentals of Aerosol Dynamics,

705 2nd Ed. ed. Oxford University Press.

706 Hand, J.L., Kreidenweis, S.M., Sherman, D.E., Jr., J.L.C., Hering, S.V., Day, D.E.,

707 Malm, W.C., 2002. Aerosol size distributions and visibility estimates during the

708 Big Bend regional aerosol and visibility observational (BRAVO) study. Atmos.

709 Environ. 36, 5043–5055. https://doi.org/10.1016/s1352-2310(02)00568-x

710 Heim, M., Kasper, G., Reischl, G.P., Gerhart, C., 2004. Performance of a new

711 commercial electrical mobility spectrometer. Aerosol Sci. Technol. 38, 3–14.

712 https://doi.org/10.1080/02786820490519252

713 Henry, R., Norris, G.A., Vedantham, R., Turner, J.R., 2009. Source region

714 identification using kernel smoothing. Environ. Sci. Technol. 43, 4090–4097.

715 https://doi.org/10.1021/es8011723

716 Hopke, P.K., Feng, Y., Dai, Q., 2022. Source apportionment of particle number

717 concentrations: A global review. Sci. Total Environ. 819, 153104.

718 http://dx.doi.org/10.1016/j.scitotenv.2022.153104

719 Hsu, C.-H., Cheng, F.-Y., 2019. Synoptic weather patterns and associated air

720 pollution in Taiwan. Aerosol Air Qual. Res. 19, 1139–1151.

721 https://doi.org/10.4209/aaqr.2018.09.0348

722 Hsu, C.-H., Cheng, F.-Y., 2016. Classification of weather patterns to study the

723 influence of meteorological characteristics on $PM_{2.5}$ concentrations in Yunlin

724 County, Taiwan. Atmos. Environ. 144, 397–408.

725 https://doi.org/10.1016/j.atmosenv.2016.09.001

726 Hu, S., Zhao, G., Tan, T., Li, C., Zong, T., Xu, N., Zhu, W., Hu, M., 2021. Current

727 challenges of improving visibility due to increasing nitrate fraction in $PM_{2.5}$ during

728 the haze days in Beijing, China. Environ. Pollut. 290, 118032.

729 https://doi.org/10.1016/j.envpol.2021.118032

730 Hu, Y., Yao, L., Cheng, Z., Wang, Y., 2017. Long-term atmospheric visibility trends

731 in megacities of China, India and the United States. Environ. Res. 159, 466–473.

732 https://doi.org/10.1016/j.envres.2017.08.018

733 Kumar, P., Morawska, L., Birmili, W., Paasonen, P., Hu, M., Kulmala, M., Harrison,

734 R.M., Norford, L., Britter, R., 2014. Ultrafine particles in cities. Environ. Int. 66,

735 1–10. https://doi.org/10.1016/j.envint.2014.01.013

736 Lee, S., Gordon, H., Yu, H., Lehtipalo, K., Haley, R., Li, Y., Zhang, R., 2019. New

737 particle formation in the atmosphere: From molecular clusters to global climate. J.

738 Geophys. Res. 124, 7098–7146. https://doi.org/10.1029/2018jd029356

739   Leoni, C., Pokorná, P., Hovorka, J., Masiol, M., Topinka, J., Zhao, Y., Křůmal, K.,
740   Cliff, S., Mikuška, P., Hopke, P.K., 2018. Source apportionment of aerosol
741   particles at a European air pollution hot spot using particle number size
742   distributions and chemical composition. Environ. Pollut. 234, 145–154.
743   https://doi.org/10.1016/j.envpol.2017.10.097

744   Li, C., Martin, R.V., 2018. Decadal changes in seasonal variation of atmospheric haze
745   over the eastern United States: Connections with anthropogenic emissions and
746   implications for aerosol composition. Environ. Sci. Technol. Lett. 5, 413–418.
747   https://doi.org/10.1021/acs.estlett.8b00295

748   Lin, G.-Y., Lee, G.-R., Lin, S.-F., Hung, Y.-H., Li, S.-W., Wu, G.-J., Ye, H., Huang,
749   W., Tsai, C.-J., 2015. Ultrafine particles and $PM_{2.5}$ at three urban air monitoring
750   stations in northern Taiwan from 2011 to 2013. Aerosol Air Qual. Res. 1–15.
751   https://doi.org/10.4209/aaqr.2015.04.0271

752   Malm, W.C., Sisler, J.F., Huffman, D., Eldred, R.A., Cahill, T.A., 1994. Spatial and
753   seasonal trends in particle concentration and optical extinction in the United States.
754   J. Geophys. Res. 99, 1347–1370.

755   Masiol, M., Vu, T.V., Beddows, D.C.S., Harrison, R.M., 2016. Source apportionment
756   of wide range particle size spectra and black carbon collected at the airport of
757   Venice (Italy). Atmos. Environ. 1994 139, 56–74.
758   https://doi.org/10.1016/j.atmosenv.2016.05.018

759   Morawska, L., Ristovski, Z., Jayaratne, E.R., Keogh, D.U., Ling, X., 2008. Ambient
760   nano and ultrafine particles from motor vehicle emissions: Characteristics, ambient
761   processing and implications on human exposure. Atmos. Environ. 42, 8113–8138.
762   https://doi.org/10.1016/j.atmosenv.2008.07.050

763   Morawska, L., Thomas, S., Jamriska, M., Johnson, G., 1999. The modality of particle
764   size distributions of environmental aerosols. Atmos. Environ. 33, 4401–4411.
765   https://doi.org/10.1016/s1352-2310(99)00217-4

766   Ogulei, D., Hopke, P., Chalupa, D., Utell, M., 2007. Modeling source contributions to
767   submicron particle number concentrations measured in Rochester, New York.
768   Aerosol Sci. Technol. 41, 179–201. https://doi.org/10.1080/02786820601116012

769   Ogulei, D., Hopke, P.K., Wallace, L.A., 2006. Analysis of indoor particle size
770   distributions in an occupied townhouse using positive matrix factorization. Indoor
771   Air 16, 204–215. https://doi.org/10.1111/j.1600-0668.2006.00418.x

772   Ogulei, D., Hopke, P.K., Zhou, L., Pancras, J.P., Nair, N., Ondov, J.M., 2006. Source
773   apportionment of Baltimore aerosol from combined size distribution and chemical
774   composition data. Atmos. Environ. 40, 396–410.
775   https://doi.org/10.1016/j.atmosenv.2005.11.075

776   Paatero, P., 1999. The multilinear engine—A table-driven, least squares program for
777   solving multilinear problems, including the n-way parallel factor analysis model. J.
778   Comput. Graph. Stat. 8, 854–888.
779   https://doi.org/10.1080/10618600.1999.10474853

780   Paatero, P., 1997. Least squares formulation of robust non-negative factor analysis.
781   Chemom. Intell. Lab. Syst. 37, 23–35. https://doi.org/10.1016/s0169-
782   7439(96)00044-5

783   Paatero, P., Hopke, P.K., 2009. Rotational tools for factor analytic models. J.
784   Chemometr. 23, 91–100. https://doi.org/10.1002/cem.1197

785   Paatero, P., Hopke, P.K., 2003. Discarding or downweighting high-noise variables in
786   factor analytic models. Anal. Chim. Acta 490, 277–289.
787   https://doi.org/10.1016/s0003-2670(02)01643-4

788   Petit, J.E., Favez, O., Albinet, A., Canonaco, F., 2017. A user-friendly tool for
789   comprehensive evaluation of the geographical origins of atmospheric pollution:
790   Wind and trajectory analyses. Environ. Model. Softw. 88, 183–187.
791   https://doi.org/10.1016/j.envsoft.2016.11.022

792   Pitchford, M., Maim, W., Schichtel, B., Kumar, N., Lowenthal, D., Hand, J., 2007.
793   Revised algorithm for estimating light extinction from IMPROVE particle
794   speciation data. J. Air Waste Manage. 57, 1326–1336.
795   https://doi.org/10.3155/uawm20.v057.i11

796   Pope, C.A., Coleman, N., Pond, Z.A., Burnett, R.T., 2020. Fine particulate air
797   pollution and human mortality: 25+ years of cohort studies. Environ. Res. 183,
798   108924. https://doi.org/10.1016/j.envres.2019.108924

799   Rivas, I., Beddows, D.C.S., Amato, F., Green, D.C., Järvi, L., Hueglin, C., Reche, C.,
800   Timonen, H., Fuller, G.W., Niemi, J.V., Pérez, N., Aurela, M., Hopke, P.K.,
801   Alastuey, A., Kulmala, M., Harrison, R.M., Querol, X., Kelly, F.J., 2020. Source
802   apportionment of particle number size distribution in urban background and traffic
803   stations in four European cities. Environ. Int. 135, 105345.
804   https://doi.org/10.1016/j.envint.2019.105345

805   Rönkkö, T., Kuuluvainen, H., Karjalainen, P., Keskinen, J., Hillamo, R., Niemi, J.V.,
806   Pirjola, L., Timonen, H.J., Saarikoski, S., Saukko, E., Järvinen, A., Silvennoinen,
807   H., Rostedt, A., Olin, M., Yli-Ojanperä, J., Nousiainen, P., Kousa, A., MASO,
808   M.D., 2017. Traffic is a major source of atmospheric nanocluster aerosol. Proc.
809   Natl. Acad. Sci. U.S.A. 114, 7549–7554. https://doi.org/10.1073/pnas.1700830114

810   Santoso, M., Hopke, P.K., Damastuti, E., Lestiani, D.D., Kurniawati, S., Kusmartini,
811   I., Prakoso, D., Kumalasari, D., Riadi, A., 2022. The air quality of Palangka Raya,
812   central Kalimantan, Indonesia: The impacts of forest fires on visibility. J. Air
813   Waste Manage. https://doi.org/10.1080/10962247.2022.2077474

814   Seinfeld, J.H., Pandis, S.N., 2016. Atmospheric Chemistry and Physics: From Air
815   Pollution to Climate Change, 3rd Ed. Wiley.
816   Singh, A., Bloss, W.J., Pope, F.D., 2017. 60 years of UK visibility measurements:
817   impact of meteorology and atmospheric pollutants on visibility. Atmos. Chem.
818   Phys. 17, 2085–2101. https://doi.org/10.5194/acp-17-2085-2017
819   Stein, A.F., Draxler, R.R., Rolph, G.D., Stunder, B.J.B., Cohen, M.D., Ngan, F.,
820   2015. NOAA's HYSPLIT atmospheric transport and dispersion modeling system.
821   Bull. Amer. Meteor. Soc. 2059–2077. https://doi.org/10.1175/bams-d-14-00110.1
822   Sun, Y., He, Y., Kuang, Y., Xu, W., Song, S., Ma, N., Tao, J., Cheng, P., Wu, C., Su,
823   H., Cheng, Y., Xie, C., Chen, C., Lei, L., Qiu, Y., Fu, P., Croteau, P., Worsnop,
824   D.R., 2020. Chemical differences between PM_1 and $PM_{2.5}$ in highly polluted
825   environment and implications in air pollution studies. Geophys. Res. Lett. 47,
826   e2019GL08628. https://doi.org/10.1029/2019gl086288
827   Sun, Y., Zhou, X., Wang, W., 2016. Aerosol size distributions during haze episodes in
828   winter in Jinan, China. Particuology 28, 1–9.
829   https://doi.org/10.1016/j.partic.2015.12.001
830   Ting, Y.-C., Young, L.-H., Lin, T.-H., Tsay, S.-C., Chang, K.-E., Hsiao, T.-C., 2021.
831   Quantifying the impacts of $PM_{2.5}$ constituents and relative humidity on visibility
832   impairment in a suburban area of eastern Asia using long-term in-situ
833   measurements. Sci. Total Environ. 151759.
834   https://doi.org/10.1016/j.scitotenv.2021.151759
835   Vu, T.V., Delgado-Saborit, J.M., Harrison, R.M., 2015. Review: Particle number size
836   distributions from seven major sources and implications for source apportionment
837   studies. Atmos. Environ. 122, 114–132.
838   https://doi.org/10.1016/j.atmosenv.2015.09.027
839   Wang, P., Cao, J., Tie, X., Wang, G., Li, G., Hu, T., Wu, Y., 2015. Impact of
840   meteorological parameters and gaseous pollutants on $PM_{2.5}$ and PM_{10} mass
841   concentrations during 2010 in Xi'an, China. Aerosol Air Qual. Res. 15, 1844–
842   1854. https://doi.org/10.4209/aaqr.2015.05.0380
843   Wang, Y.Q., Zhang, X.Y., Sun, J.Y., Zhang, X.C., Che, H.Z., Li, Y., 2015. Spatial
844   and temporal variations of the concentrations of PM_{10}, $PM_{2.5}$ and PM_1 in China.
845   Atmos. Chem. Phys. 15, 13585–13598. https://doi.org/10.5194/acp-15-13585-2015
846   Wang, Z., Wu, Z., Yue, D., Shang, D., Guo, S., Sun, J., Ding, A., Wang, L., Jiang, J.,
847   Guo, H., Gao, J., Cheung, H.C., Morawska, L., Keywood, M., Hu, M., 2017. New
848   particle formation in China: Current knowledge and further directions. Sci. Total
849   Environ. 577, 258–266. https://doi.org/10.1016/j.scitotenv.2016.10.177
850   Xia, Y., Tao, J., Zhang, L., Zhang, R., Li, S., Wu, Y., Cao, J., Wang, X., Ma, Q.,
851   Xiong, Z., 2017. Impact of size distributions of major chemical components in fine

852   particles on light extinction in urban Guangzhou. Sci. Total Environ. 587–588, 1–

853   8. https://doi.org/10.1016/j.scitotenv.2017.02.127

854 Yi, H., Zhang, J., Xiao, H., Tong, L., Cai, Q., Lin, J., Yu, W., Johnson, M.S., 2020.

855   Compact algorithms for predicting of atmospheric visibility using $PM_{2.5}$, relative

856   humidity and NO_2. Aerosol Air Qual. Res. 20, 679–687.

857   https://doi.org/10.4209/aaqr.2019.06.0286

858 Young, L.-H., Lee, S.H., Kanawade, V.P., Hsiao, T.C., Lee, Y.L., Hwang, B.F., Liou,

859   Y.J., Hsu, H.T., Tsai, P.J., 2013. New particle growth and shrinkage observed in

860   subtropical environments. Atmos. Chem. Phys. 13, 547–564.

861   https://doi.org/10.5194/acp-13-547-2013

862 Young, L.-H., Wang, Y.-T., Hsu, H.-C., Lin, C.-H., Liou, Y.-J., Lai, Y.-C., Lin, Y.-

863   H., Chang, W.-L., Chiang, H.-L., Cheng, M.-T., 2012. Spatiotemporal variability

864   of submicrometer particle number size distributions in an air quality management

865   district. Sci. Total Environ. 425, 135–145.

866   https://doi.org/10.1016/j.scitotenv.2012.02.063

867 Yu, R.C., Teh, H.W., Jaques, P.A., Sioutas, C., Froines, J. R., 2004. Quality control of

868   semi-continuous mobility size-fractionated particle number concentration data.

869   Atmos. Environ. 38, 3341–3348. https://doi.org/10.1016/j.atmosenv.2004.03.009

870 Yue, W., Stölzel, M., Cyrys, J., Pitz, M., Heinrich, J., Kreyling, W.G., Wichmann,

871   H.E., Peters, A., Wang, S., Hopke, P.K., 2008. Source apportionment of ambient

872   fine particle size distribution using positive matrix factorization in Erfurt,

873   Germany. Sci. Total Environ. 398, 133–144.

874   https://doi.org/10.1016/j.scitotenv.2008.02.049

875

876

877

878

Table 1. Summary statistics of measured aerosol light scattering (b_{sp}), absorption (b_{ap})

and extinction (b_p) (Mm^{-1}).

	b_{sp}	b_{ap}	b_p
Mean	65.2	22.9	88.3
SD	56.0	18.1	69.2
RSD	0.86	0.79	0.78
Q1	15.7	8.3	24.0
Q2	37.0	15.1	52.1
Q3	67.2	25.0	92.2
Q4	143.5	41.5	185.0

The 1st, 2nd and 3rd quartiles of b_p were used to divide the data into 4 quarters, Q1, Q2,

Q3 and Q4.

883

Table 2. The particle number (PN) mode, mode diameter, peak PN hour, source region and wind condition for each source type.

Factor	Source type	Particle number mode[a]	Mode diameter(s) (nm)	Peak hour(s) (Local time)	Source region	Wind condition
F1	Transport of primary emission and secondary formation	Nucleation	**16**[b]	0800, **1300**[b]	SW	> 2.2 m s^{-1}
F2	Transport of regional aerosols	"Large" Aitken	<15, **69**, 261	**1600**	NW, N, NE	> 1.1 m s^{-1}
F3	Build-up of local aged aerosols	"Large" accumulation	23, 92, **377**	**0800**	Local	< 1.1 m s^{-1} (stagnant)
F4	Aerosol growth from F1	"Small" Aitken	**40**	**1200**	SW	> 2.2 m s^{-1}
F5	Local aerosols and transport of SO$_2$-related aerosols	"Large" Aitken	**84**	0800, 1200, **2000**	Local, NW	< 1.1 m s^{-1} (Local) > 1.1 m s^{-1} (NW)
F6	Build-up of local aerosols (daytime) and growth from F5 (nighttime)	"Small" accumulation	33, **168**	**0800**	Local, NW	< 1.1 m s^{-1} (Local) > 1.1 m s^{-1} (NW)

[a]The size range of nucleation mode is < 25 nm, small Aitken mode is $25 - 50$ nm, large Aiken mode is $50 - 100$ nm, small accumulation mode is $100 - 300$ nm, and large accumulation mode is $300 - 1000$ nm.

[b]Bold numbers represent the most prominent mode diameter and peak hour.

Table 3. The correlation coefficients between the PMF-resolved factor particle number (PN) concentrations, air pollutants and meteorological parameters.

	F1TPN	F2TPN	F3TPN	F4TPN	F5TPN	F6TPN
F1TPN	1.00					
F2TPN	-0.08	1.00				
F3TPN	-0.13	-0.25	1.00			
F4TPN	**0.45**	-0.11	-0.03	1.00		
F5TPN	0.11	**-0.46**	0.28	0.36	1.00	
F6TPN	0.05	-0.27	**0.50**	0.18	**0.64**	1.00
CPM	0.03	-0.06	0.36	0.18	**0.37**	0.44
FPM	-0.08	-0.22	0.64	0.06	0.50	**0.69**
b_{sp}	-0.13	-0.21	**0.65**	-0.01	0.44	0.61
b_{ap}	0.11	-0.32	0.56	0.26	**0.67**	0.72
SO_2	0.16	-0.24	0.23	0.23	**0.49**	0.43
O_3	**0.31**	-0.06	0.12	0.22	-0.07	0.07
NO	0.13	**-0.42**	0.22	0.16	0.33	0.27
RH	**-0.32**	-0.21	0.12	-0.29	0.04	-0.04
WS	0.14	**0.56**	-0.26	0.06	-0.33	-0.23
UVI	**0.40**	0.15	-0.04	0.29	-0.06	-0.03

Bold numbers are those with the strongest correlations between two variables.
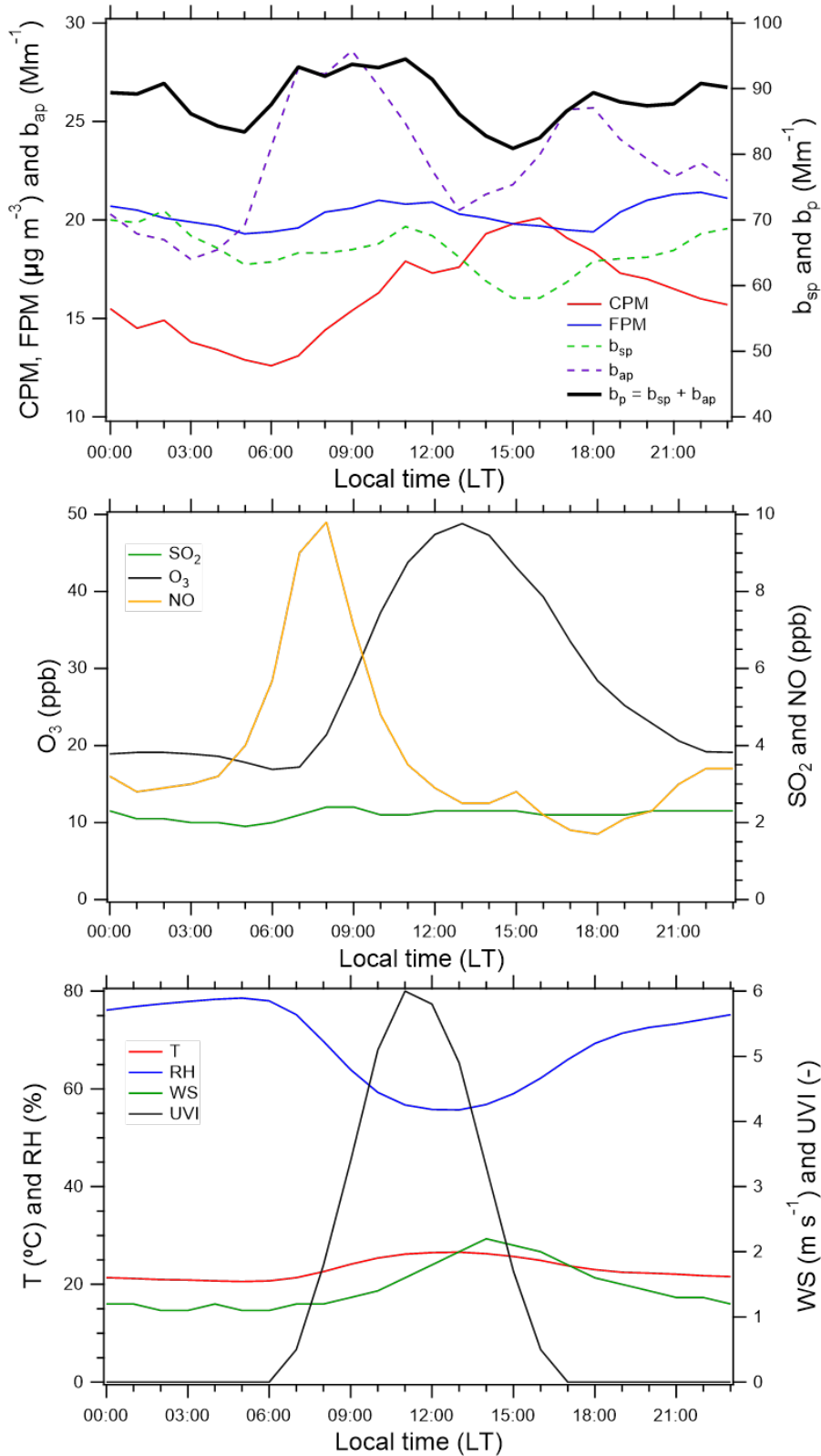
Fig. 1. The diurnal variations of aerosol parameters (CPM, FPM, b_{sp}, b_{ap}, b_p), gas pollutants (SO_2, O_3, NO) and meteorological parameters (T, RH, WS and UVI).
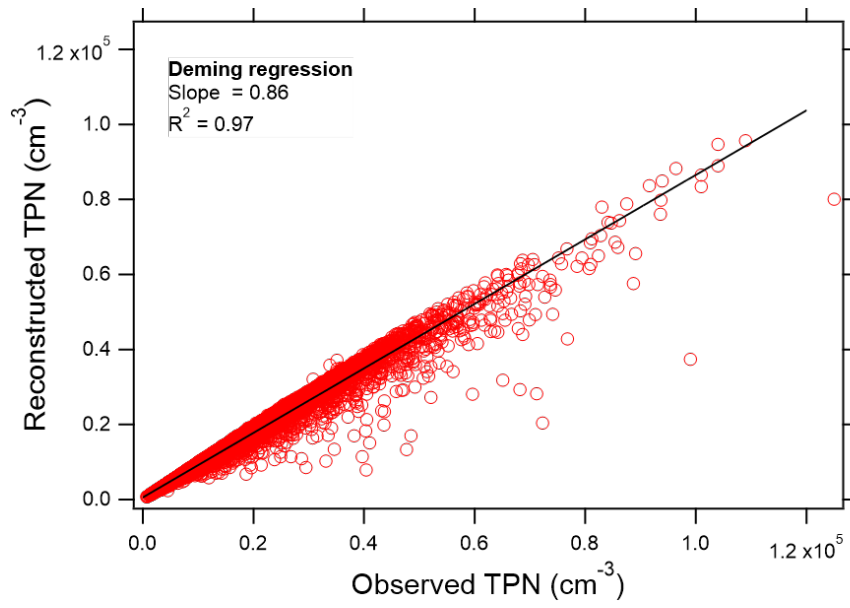
Fig. 2. The PMF-reconstructed total particle number (TPN) concentration versus the observed TPN.
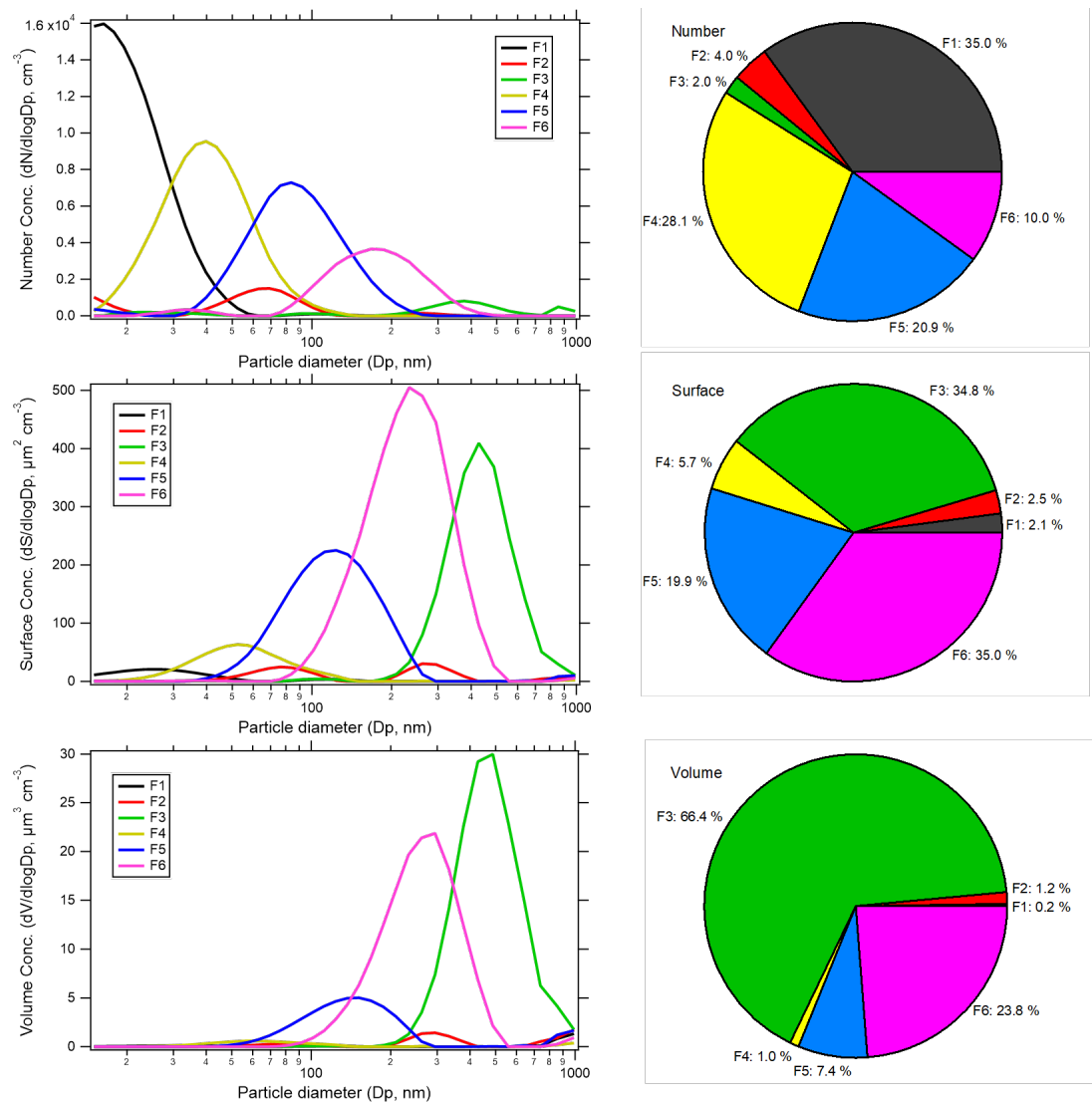
Fig. 3. The PMF-resolved particle number, surface and volume size distribution profiles of the six factors and their contributions to the total particle number (TPN), surface (TPS) and volume (TPV).
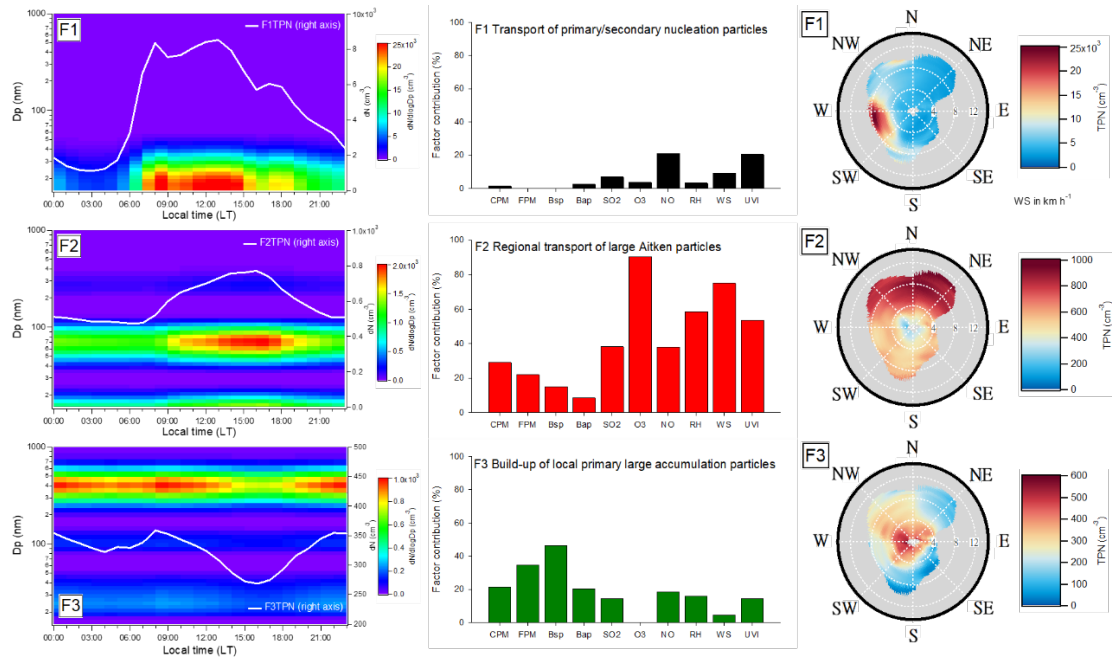
Fig. 4. The diurnal variation of the PMF-resolved average particle number size distributions (PNSDs) and total particle number concentrations (TPNs), factor loadings and non-parametric wind regression (NWR) plots of F1, F2 and F3.
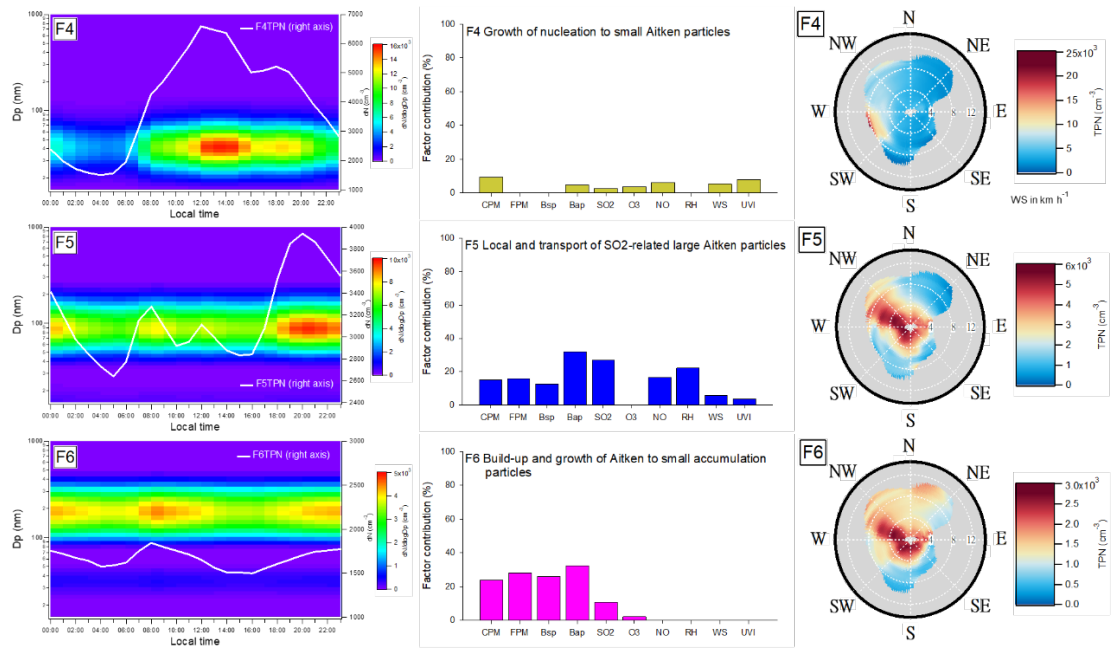
Fig. 5. The diurnal variation of the PMF-resolved average particle number size distributions (PNSDs) and total particle number concentrations (TPNs), factor loadings and non-parametric wind regression (NWR) plots of F4, F5 and F6.
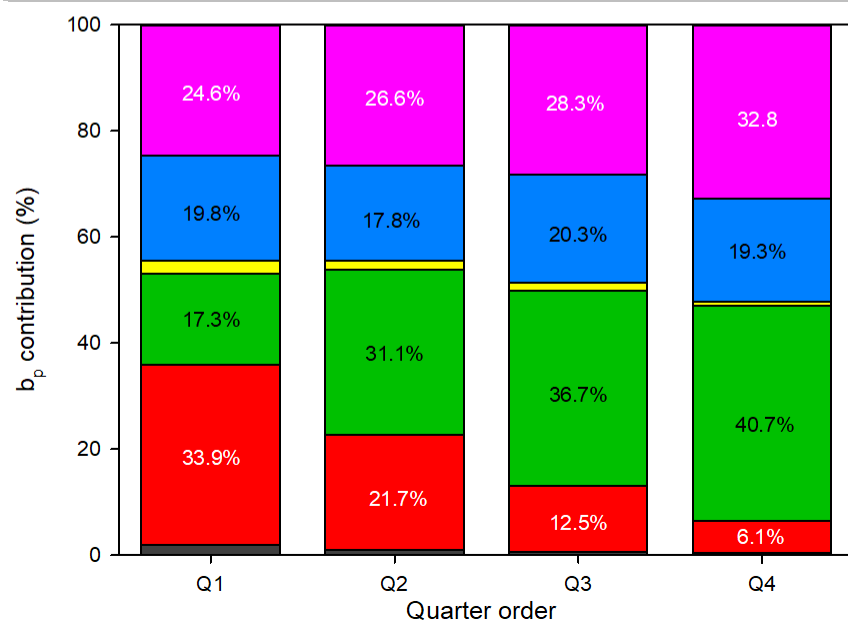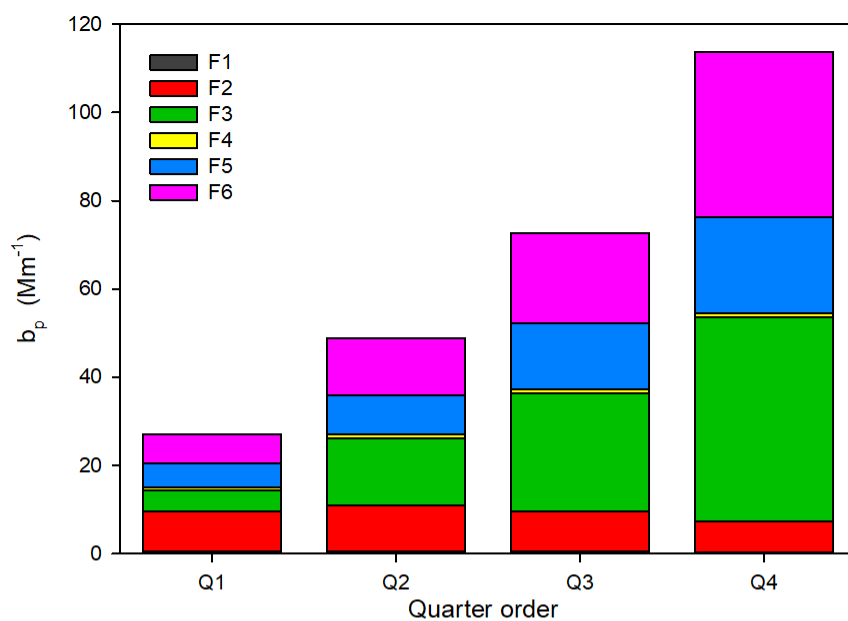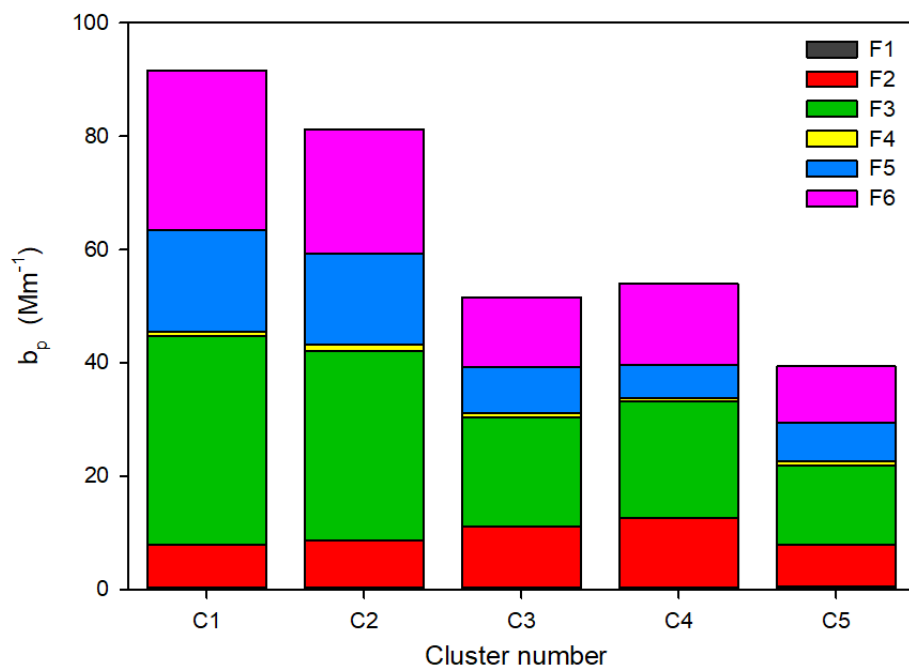
Fig. 6. The aerosol extinction coefficient ($b_p = b_{sp} + b_{ap}$) and b_p-contributions associated with the PMF-resolved six factors under different visibility classes; the first quarter (Q1) represents the best visibility, whereas the fourth quarter (Q4) represents the poorest visibility.
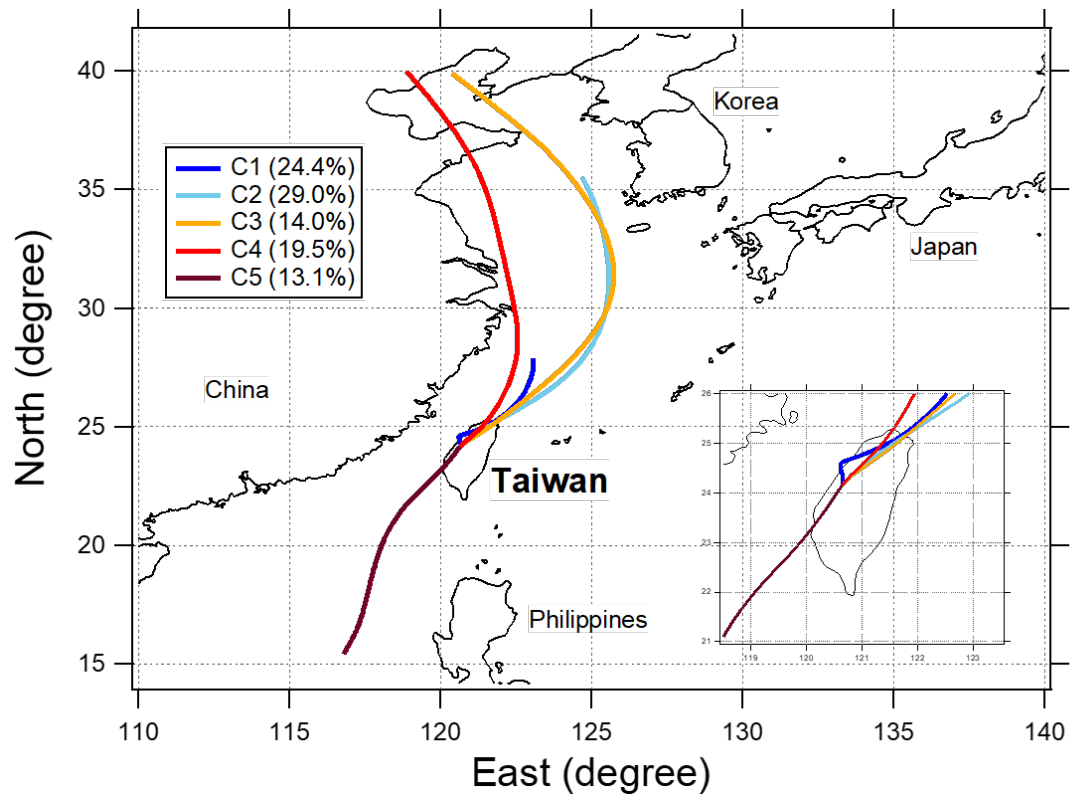
Fig. 7. The five representative clusters of 72-hr air-mass back trajectory during the study period.
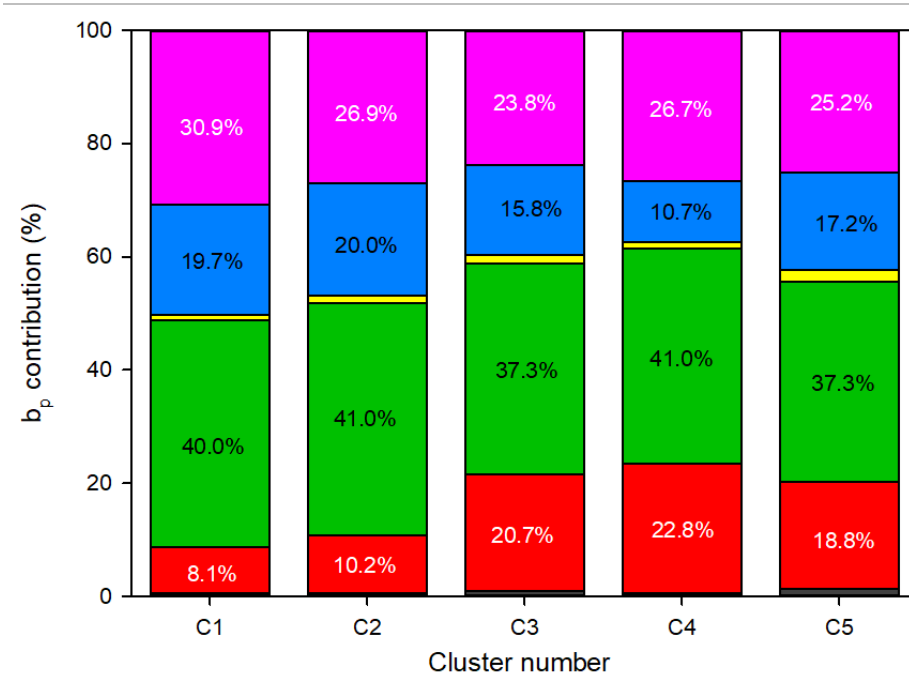
Fig. 8. The aerosol extinction coefficient ($b_p = b_{sp} + b_{ap}$) and b_p-contributions associated with the PMF-resolved six factors for each air-mass back trajectory cluster

Supplemental Information

Table S1. Summary statistics of the meteorological parameters and air quality during the study period.

	Mean	SD	RSD
TEMP (°C)	23.1	5.3	0.23
RH (%)	69.1	13.5	0.20
WS (m s^{-1})	1.5	0.7	0.48
UVI	1.4	2.3	1.69
PM$_{10}$ (μg m^{-3})	35.2	21.6	0.61
CPM (=PM$_{10}$ – PM$_{2.5}$; μg m^{-3})	16.3	11.0	0.68
FPM (PM$_{2.5}$; μg m^{-3})	20.3	13.2	0.65
SO$_2$ (ppb)	2.2	1.2	0.56
O$_3$ (ppb)	27.9	17.5	0.63
NO (ppb)	3.7	7.3	1.94
PN$_{25}$ (cm^{-3})	7043	7208	1.02
PN$_{25-100}$ (cm^{-3})	6938	4890	0.70
PN$_{100-1000}$ (cm^{-3})	2365	1973	0.83
TPN (cm^{-3})	16347	11543	0.71

UVI is the ultraviolet index, CPM is the coarse particulate matter, FPM is the fine particulate matter, PN stands for the particle number concentration and subscript is the particle size range in nm, and TPN is the total particle number concentration.
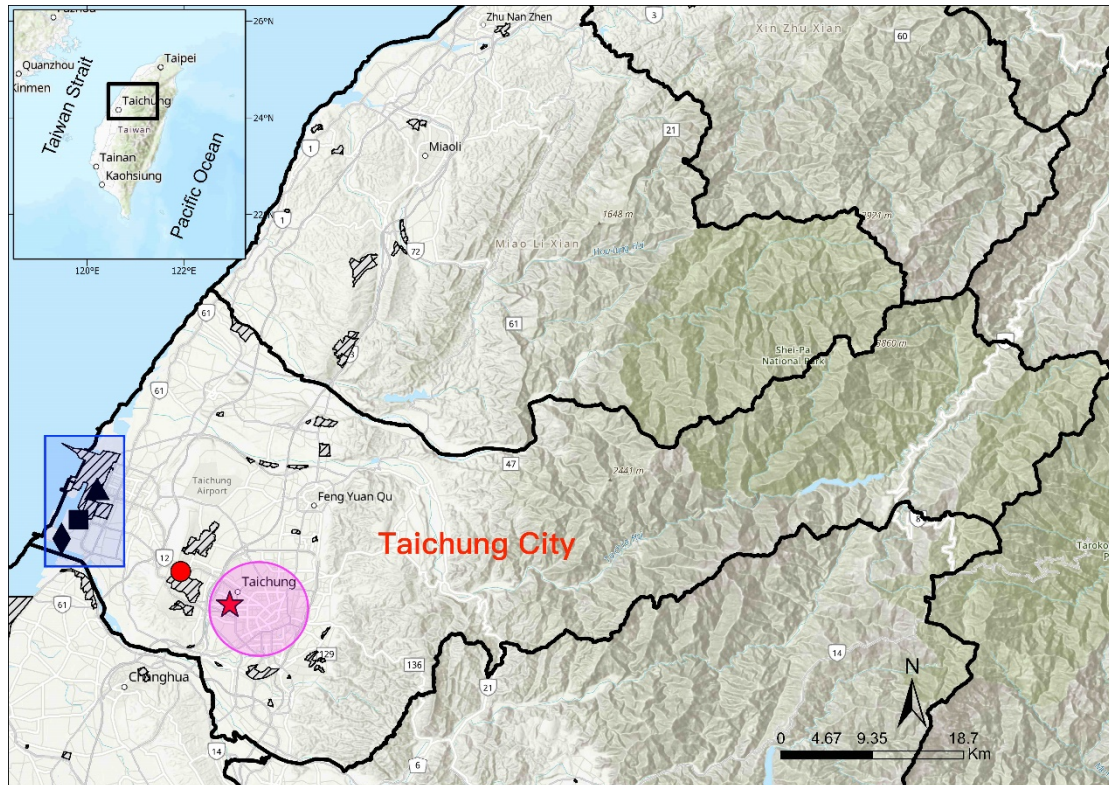
Fig. S1. A map of the study area and sampling sites (star: main site; circle: satellite site) and surrounding major stationary sources (diamond: power plant; square: steel plant; triangle: Taichung port; shaded area: industrial or science park). The shaded circle is the Taichung urban basin, whereas the shaded rectangular is an area more concentrated with large emission sources. To the right of the map lies the highest and largest terrain in Taiwan, the Central Mountain Range,
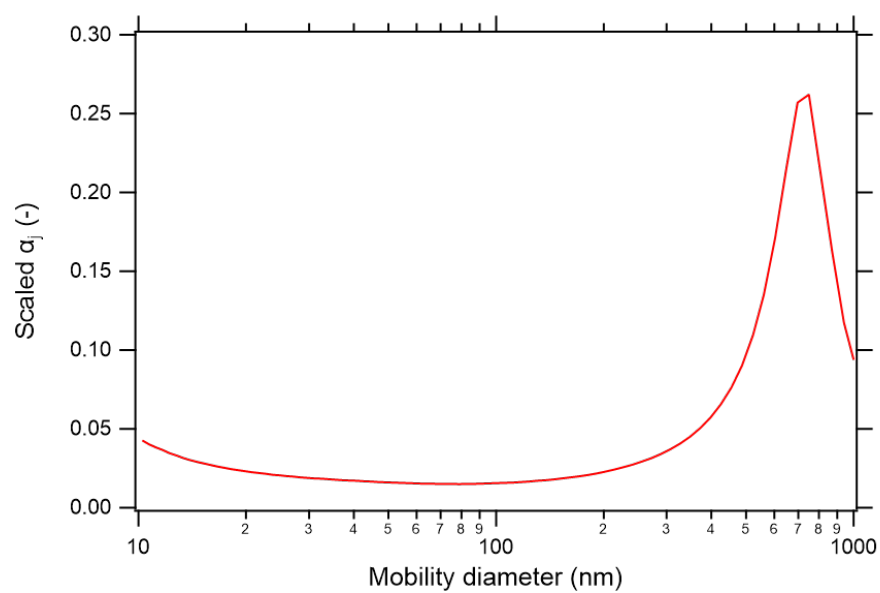
Fig. S2. The size-dependent scaled measurement (counting) uncertainty (α_j) of the measured particle number size distribution.
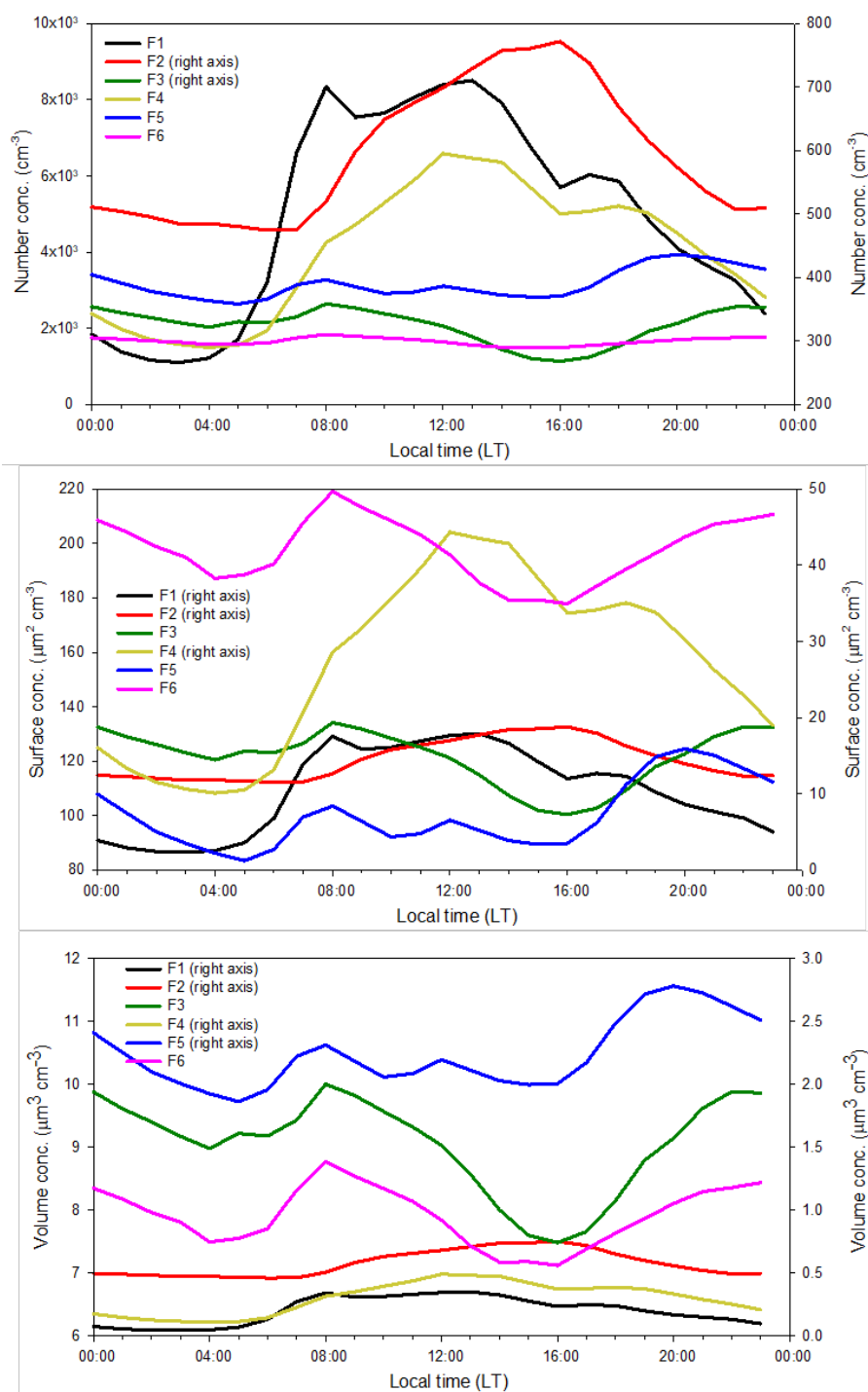
Fig. S3. The diurnal variations of the total particle number, surface and volume concentrations of the PMF-resolved six factors.
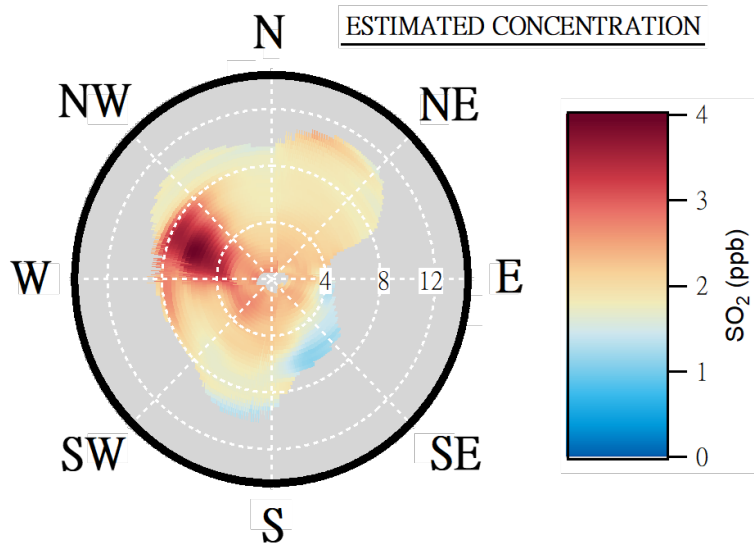
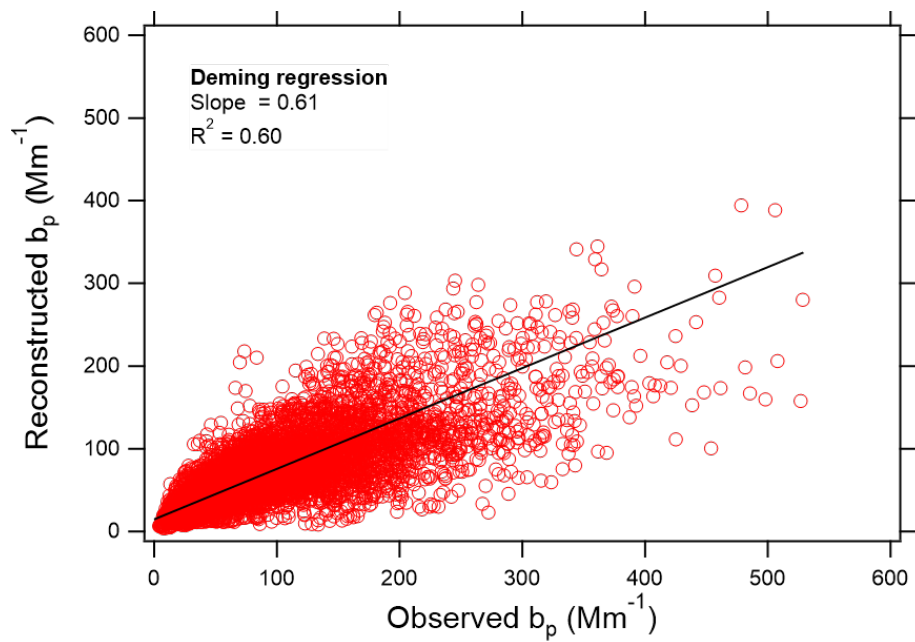**Fig. S4.** The non-parametric wind regression (NWR) plot of SO$_2$.

Fig. S5. The PMF-reconstructed aerosol extinction coefficient ($b_p = b_{sp} + b_{ap}$) versus the observed b_p.
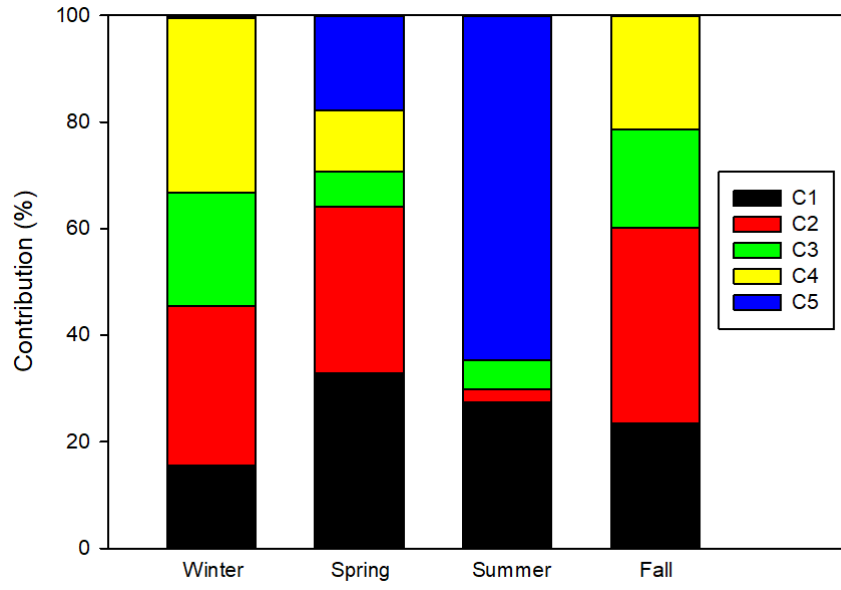
Fig. S6. The proportions of the five air-mass trajectory clusters in each season.